Article

Current Biology

FGF Pyramus Has a Transmembrane Domain and Cell-Autonomous Function in Polarity

Graphical Abstract

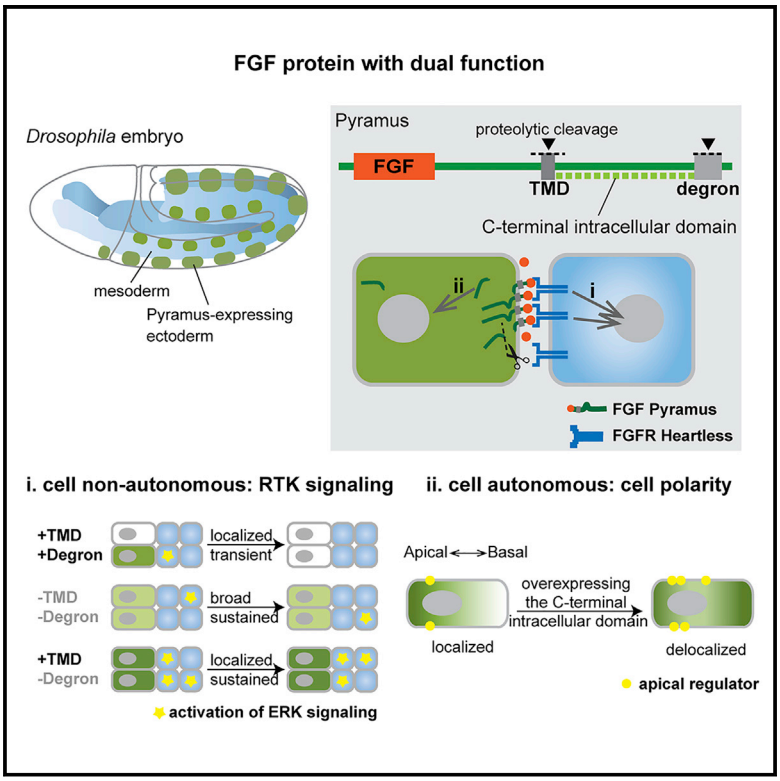

Highlights

- The *Drosophila* FGF Pyr has functional domains outside of its core FGF domain
- Transmembrane domain promotes spatial precision of Pyr signaling to its receptor Htl
- The non-secreted Pyr intracellular domain controls the distribution and levels of Pyr
- The intracellular domain of Pyr regulates cell polarity in a cell-autonomous manner

Authors

Vincent Stepanik, Jingjing Sun, Angelike Stathopoulos

Correspondence

angelike@caltech.edu

In Brief

Stepanik et al. demonstrate that the *Drosophila* Pyramus (Pyr) protein harbors functional domains outside of its core FGF domain not previously identified in FGFs. A transmembrane domain promotes the spatial precision of Pyr signaling to its receptor, and C-terminal degron is required for a previously unidentified cell-autonomous role for Pyr in cell polarity.

Stepanik et al., 2020, Current Biology *30*, 3141–3153
August 17, 2020
https://doi.org/10.1016/j.cub.2020.06.006

CellPress

Current Biology

CellPress

Article

FGF Pyramus Has a Transmembrane Domain and Cell-Autonomous Function in Polarity

Vincent Stepanik,[1,2] Jingjing Sun,[1,2] and Angelike Stathopoulos[1,3,*]
[1]Division of Biology and Biological Engineering, California Institute of Technology, 1200 East California Boulevard, Pasadena, CA 91125, USA
[2]These authors contributed equally
[3]Lead Contact
*Correspondence: angelike@caltech.edu
https://doi.org/10.1016/j.cub.2020.06.006

SUMMARY

Most fibroblast growth factors (FGFs) function as receptor ligands through their conserved FGF domain, but sequences outside this domain vary and are not well studied. This core domain of 120 amino acids (aa) is flanked in all FGFs by highly divergent amino-terminal and carboxy-terminal sequences of variable length. *Drosophila* has fewer FGF genes, with only three identified to date, *pyramus* (*pyr*), *thisbe* (*ths*), and *branchless* (*bnl*), and all three encoding relatively large FGF proteins (~80 kDa). We hypothesized that the longer FGF proteins present in *Drosophila* and other organisms may relate to an ancestral form, in which multiple functions or regulatory properties are present within a single polypeptide. Here, we focused analysis on Pyr, finding that it harbors a transmembrane domain (TMD) and extended C-terminal intracellular domain containing a degron. The intracellular portion limits Pyr levels, whereas the TMD promotes spatial precision in the paracrine activation of Heartless FGF receptor. Additionally, degron deletion mutants that upregulate Pyr exhibit cell polarity defects that lead to invagination defects at gastrulation, demonstrating a previously uncharacterized cell-autonomous role. In summary, our data show that Pyr is the first demonstrated transmembrane FGF, that it has both extracellular and intracellular functions, and that spatial distribution and levels of this particular FGF protein are tightly regulated. Our results suggest that other FGFs may be membrane tethered or multifunctional like Pyr.

INTRODUCTION

The length of sequences outside the core FGF domain varies greatly among fibroblast growth factor (FGF) genes, of which 22 have been identified in vertebrates (reviewed in [1]). The N- and C-terminal flanking sequences are very short for genes FGF1, FGF2, FGF4, FGF6, FGF7, and FGF10. In contrast, extended sequences are present in FGF3, FGF5, FGF8, FGF9, and FGF16–19 and have properties such as supporting autoinhibition through homodimerization (FGF9) and even supporting nuclear localization (FGF1 and FGF2) [2, 3]. These observations suggest that FGF proteins, especially those with extended sequences, may have additional functions beyond those supported by the core FGF domain, which include receptor binding/activation.

In particular, relatively long regions of undefined functions are located at the C termini of *Drosophila* FGF proteins Pyr and Ths (Figure 1A) [4]. We showed that each contains a signal peptide at the N terminus and that the N-terminal portion of each protein is secreted into cell culture supernatants (Figures S1A and S1B) [5]. These results suggested that Ths can be secreted in entirety (but sometimes without its C terminus due to proteolytic cleavage), whereas the fate of the Pyr C terminus, which is not detectable in supernatants, was less clear.

The extracellular portions of Pyr and Ths ligands both activate the Heartless (Htl) FGF receptor [5–7]. *pyr* and *ths* have both overlapping and distinct roles in supporting Htl-dependent processes, including control of mesoderm spreading at gastrulation [8, 9]. Although *pyr* and *ths* genes usually share spatiotemporally similar expression patterns, *pyr* is generally expressed in a more restricted domain relative to *ths* [4]. Our previous study suggested an interaction between the membrane-tethered heparan sulfate proteoglycan (HSPG) syndecan with Pyr, whereas the secreted, extracellular HSPG Trol was found to genetically interact with Ths [10, 11]. Collectively, these results suggested that Pyr may signal to Htl through its FGF domain in a more localized manner, whereas Ths may have a longer range of action. Here, we investigated whether the extended Pyr sequence outside the FGF core domain contributes to its signaling potential.

RESULTS

Pyr, but Not Ths, Has a Transmembrane Domain Following Its FGF Domain

Phobius computational analysis (STAR Methods) [12] predicts a transmembrane domain (TMD) from amino acids (aa) 400–425 in Pyr, but not for Ths (Figure 1B, top versus bottom). These residues are highly conserved among *Drosophila* species and Tephritidae and Muscidae fly families, although adjacent sequences lack conservation (Figure 1C). A block of nearly invariant basic

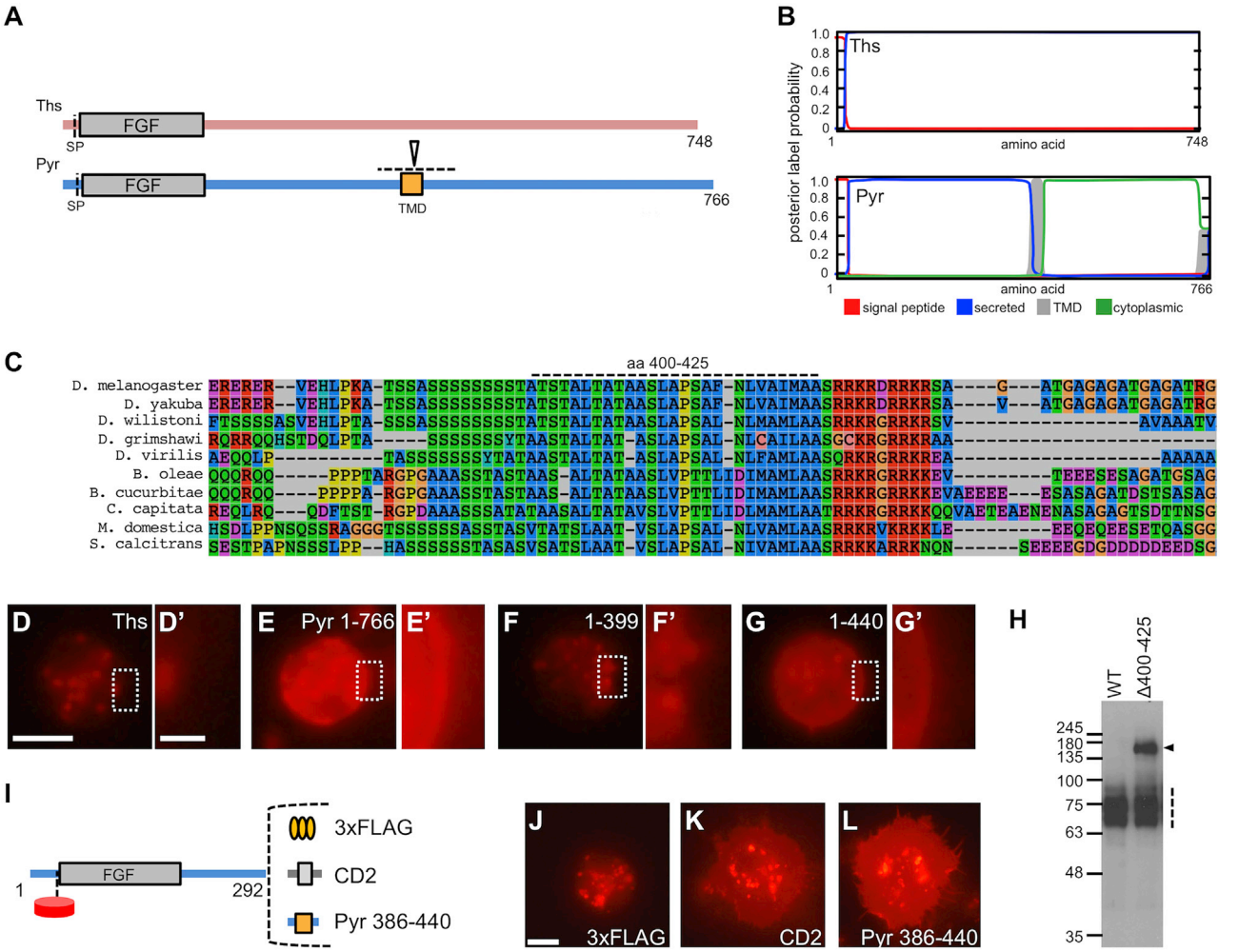

Figure 1. Pyr, but Not Ths, Has a Conserved Transmembrane Domain

(A) Domain structure of Ths and Pyr, with N-terminal FGF domains and extended C termini showing signal peptide cleavage site (SP) [5] and approximate location of a proteolytic cleavage site (arrowhead) near the transmembrane domain (TMD).

(B) Analysis of Ths and Pyr with Phobius [52] predicts a single-pass transmembrane domain in Pyr using hydrophobicity, helical structure, and post-helix amino acid context (posterior label probability; y axis) to indicate the secretory and membrane fate along the protein (x axis).

(C) MUSCLE [53] alignment using Seaview [54] of Pyr orthologs from several *Drosophila* species and other Dipteran flies (STAR Methods).

(D–G') Assay of membrane localization for indicated mCh-tagged Ths and Pyr constructs in S2 cells. Boxes indicate the cell peripheries (D–G) and regions shown enlarged in (D')–(G'). Scale bars, (D–G) 10 μm and (D'–G') 2 μm.

(H) Higher-molecular-weight isoforms (arrowhead) of Pyr are detectable in S2 cell supernatants with the N-terminal mCh tag when aa 400–425 are deleted, along with the previously seen isoforms (dashed line).

(I) Fusions of 3xFLAG, the CD2 TMD, and Pyr aa 386–440 to the tagged Pyr extracellular domain (mCh-Pyr aa 1–292) to assay for tethering capability to the plasma membrane.

(J–L) Live imaging of the constructs in (I) shows Pyr aa 386–440 tethers the extracellular domain of Pyr to the plasma membrane (L) similar to CD2 (K), but unlike 3xFLAG (J). Scale bar, 20 μm.

See also Figures S1 and S3.

residues immediately follows from R427 to R435, consistent with the "positive inside" rule for efficient membrane insertion of transmembrane helices [13, 14]. Live imaging of the mCh fusions in cell culture shows evidence of a Pyr TMD. Although both Ths and Pyr localize to vesicles in transfected cultured *Drosophila* S2 cells, Pyr also shows membrane localization (Figures 1D–1E'). Pyr 1-440 localizes to the membrane, although Pyr 1–399 does not, further indicating aa A400–A425 act as a TMD (Figures 1F–1G').

Adding this region and adjacent sequences necessary to retain the Phobius TMD prediction to a tagged portion of the extracellular domain of Pyr (i.e., mCh-Pyr aa 1–292) promotes tethering to the membrane similar to CD2 (positive control), although 3xFLAG (negative control) does not (Figures 1J–1L). Additionally, deletion of A400–A425 results in the appearance of an additional, higher-molecular-weight band in supernatants (Figure 1H), demonstrating that this sequence normally prevents secretion of the polypeptide following T425. These data

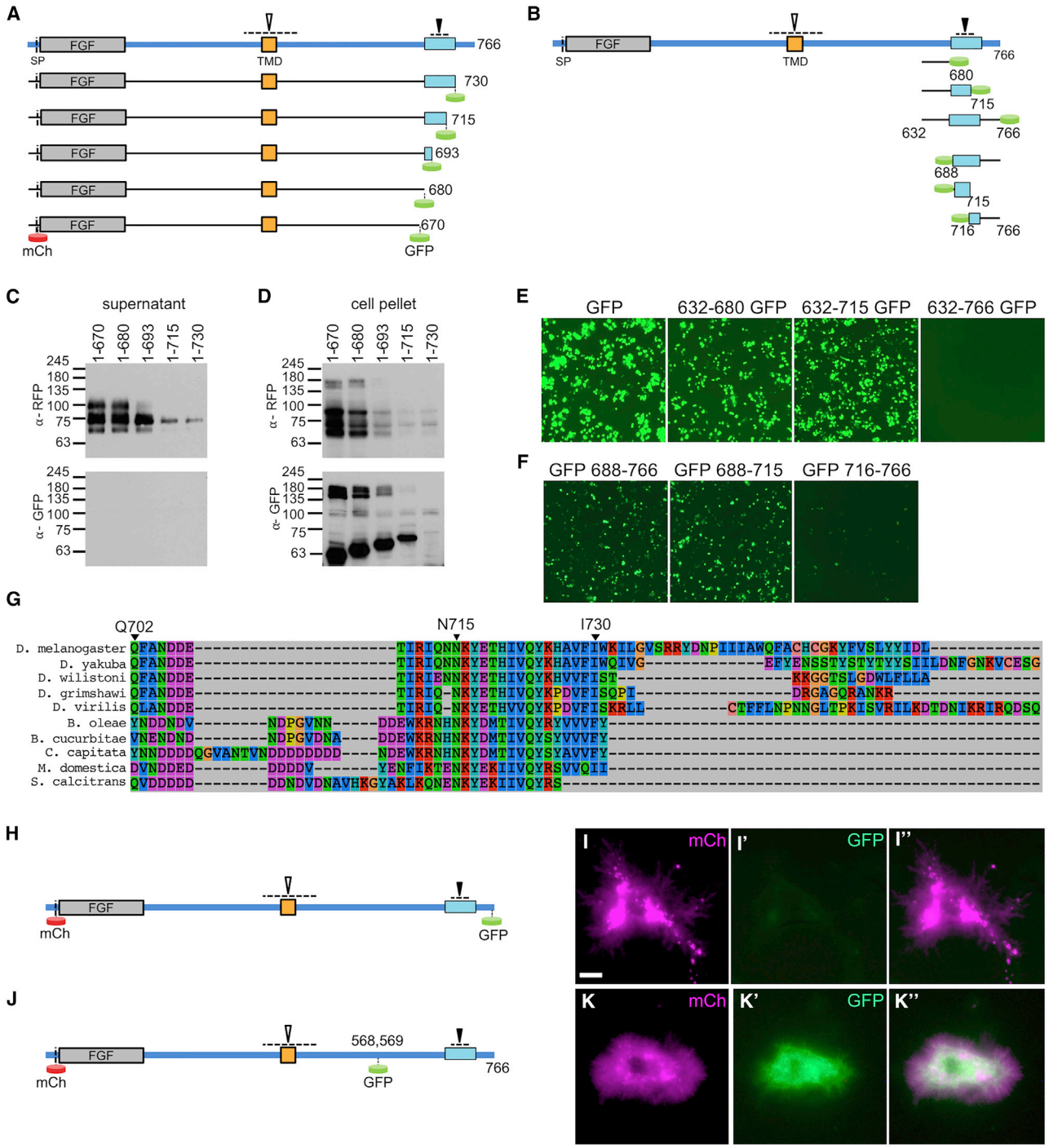

Figure 2. A Potent, Conserved Degron Is Present at the C Terminus of Pyr

(A) Pyr truncations tagged at N and C termini with mCh and GFP, respectively, to identify the degron (light blue box). In this and all subsequent figures, arrowheads and dashed lines indicate approximate sites of cleavage.

(B) The indicated Pyr fragments were fused to the N and C termini of GFP to test their ability to act as a degron, i.e., destabilize the GFP.

(C and D) Western analysis of Pyr truncations shown in (A) tagged with mCh and GFP tags at their N and C termini, respectively, for extracts made from supernatant (C) or cell pellet (D) fractions.

(E and F) The indicated Pyr C-terminal fragments as shown in (B), transfected into S2 cells and assayed for GFP signal 2 days after transfection. C-terminal GFP fusions show fragment 632–766 supports degradation (E), whereas N-terminal fusions to GFP show that fragment 716–766 is sufficient to support degradation (F).

(G) MUSCLE alignment of the highly conserved C-terminal region from residues 715–730 and less-conserved adjacent sequences of Pyr orthologs (STAR Methods).

(legend continued on next page)

demonstrate that Pyr has a TMD, a feature not previously identified in FGFs.

The C Terminus of Pyr Has a Potent Degradation Sequence

When a GFP tag (~27 kDa) is inserted at the Pyr C terminus, it is not detectable by western blot or microscopy (Figures 2A, 2C, 2D, S2A, and S2B), suggesting that the Pyr C terminus is destabilizing. To define a putative degradation sequence, we surveyed a series of truncations near the Pyr C terminus, tagged at their C termini with GFP (Figure 2A). The longest C-terminal truncation retaining GFP signal is 1–715 (Figure 2D, bottom), indicating a destabilizing sequence near aa 716–730. Total Pyr levels (i.e., extracellular/supernatant and intracellular/cell pellet) further increase when aa 681–693 or aa 694–715 are further deleted (Figures 2C and 2D, respectively), indicating a secondary degradation sequence. aa 710–730 of Pyr are highly conserved, although sequences just N-terminal to this region are less so (Figures 2G and S3).

To test whether these sequences have intrinsic degradative capacity, we expressed GFP fused to fragments of the Pyr C terminus in S2 cells (Figures 2B and 2E). Strong GFP expression is observed with all but the $Pyr^{632–766}$-GFP fusion, which shows no signal (Figure 2E). This demonstrates that residues 716–766 support efficient degradation as a "degron" (Figures 2A, 2C, and 2D) that is portable to non-Pyr proteins and effective even outside of the secretory pathway. Despite the potent degradative capacity of these residues, the N terminus of Pyr remains detectable when expressed in the context of full-length protein (e.g., Figures 2C and S1B–S1D, top, 1–766). It is therefore likely that this degron is cleaved from the rest of Pyr. In support of this, fusion of either aa 688–766 or 688–715 to the C terminus of GFP downregulates but does not eliminate GFP fluorescence, whereas fusion to aa 716–766 does (Figure 2F).

Interestingly, when GFP is inserted in frame within Pyr^{intra} between the TMD and C-terminal degron, signal is detected (i.e., stable within the context of full-length Pyr), but not when placed at the very C terminus (Figure 2I' versus Figure 2K'). It is associated with mCh signal in vesicles and at cellular protrusions and independently in the cytoplasm and in vesicles, indicating that cleavage from the N terminus occurs intracellularly (Figure 2K").

Intracellular Pyr Is Separable from the N Terminus and Is Detectable *In Vivo*

To characterize Pyr^{intra}, we generated an antibody to aa 452–715 (Figure 3A). Anti-Pyr^{intra} recognizes 140–170 kDa isoforms in S2 cells transfected with dual-tagged Pyr that correspond to the same bands recognized when detecting the N terminus, indicative of full-length protein (i.e., $Pyr^{N\text{-}term}$+Pyr^{intra}; Figures 3B and S1E; compare with Figure S1D cell pellet, anti-RFP). Lower-molecular-weight Pyr^{intra} bands separated from the N-terminal fragments are also detected for the full-length and truncation constructs and, in the case of full length, separate from the C-terminal degron (i.e., ~50 kDa for 1–680 and ~52 kDa for 1–766; Figure 3B).

Pyr^{intra} was not readily detectable by western blot in extracts from a variety of developmental time points (e.g., embryo, larva, adult, and ovary), indicating that it is expressed at low levels, likely due to the presence of the C-terminal degron. We therefore enriched for Pyr^{intra} through immunoprecipitation (IP) from 3- to 7-h embryo extracts, a window in which Pyr function has been characterized [8, 15]. Pyr^{intra} was detected as a smear from 49–57 kDa, shorter than if present as full-length Pyr or still connected to the TMD, neither of which are expected to be extracted by our IP-compatible conditions (Figure 3C; Pyr 1–430; see below). The resulting smear of the Pyr^{intra}-specific signal may relate to post-translational modification(s) or the lability of Pyr^{intra} at this stage. When Pyr^{intra} was immunoprecipitated from extracts of S2 cells constitutively expressing full-length Pyr, similar signal was detected with a predominant band of ~57 kDa that was absent from control S2 cells (Figure 3D).

Pyr Truncation Mutants Exhibit Phenotypes Including Increased Survivability Consistent with Gain of Function

To test the functional significance of the TMD and degron of Pyr *in vivo*, we introduced stop codons into the endogenous *pyr* locus to remove the functions of these domains using the CRISPR-Cas9 system (STAR Methods) [16]. pyr^{399} and pyr^{430} both delete Pyr^{intra}, although pyr^{399} also deletes the TMD (Figure 3E). pyr^{715} removes the potent degron, although pyr^{680} removes additional sequence that further reduces total Pyr and Pyr^{intra} levels in cultured S2 cells when present (Figure 3E; see also Figure 2D).

pyr-null mutants that delete the entire gene coding sequence are lethal [17]. All *pyr* mutants that delete the TMD and/or intracellular domain created by CRISPR-Cas9 are viable and fertile, suggesting that loss of Pyr N-terminal function is the underlying cause of the lethality of null mutants. However, these *pyr* truncation mutants are severely compromised in health and exhibit decreased fertility, with some stocks producing less than 25% of the expected progeny (i.e., pyr^{715}), requiring the stocks be kept as heterozygotes (i.e., over balancer; STAR Methods). When *pyr* mutations are assayed in *trans* to a *pyr*-null allele (i.e., *Df(2R)pyr36*) [17], pyr^{430}/*Df* and pyr^{680}/*Df* display a better survival rate compared to +/*Df* (Figure 3H).

Using the Pyr^{intra} antibody, no staining is observed in pyr-null embryos (i.e., *Df(2R)pyr36*) or the C-terminal truncation (i.e., pyr^{399} and pyr^{430}) mutants (Figures 3K and 3M), demonstrating antibody specificity. This antibody detects in wild-type embryos a pattern indistinguishable from the highly dynamic pyr *in situ* pattern (Figures 3I–3J'; compared with Figures 3F–3G') [4]. Furthermore, anti-Pyr^{intra} staining appears to be stronger in the mutant that lacks the C-terminal degron (i.e., pyr^{680}; Figure 3L versus Figure 3J), suggesting that Pyr^{680} protein, and likely also Pyr^{430}, may be expressed at higher levels due to lack of the C-terminal degron.

(H–K") Schematics and S2 cell fluorescence signals associated with dual fluor-tagged Pyr with GFP either at the C terminus (H and I–I") or in frame between H568 and S569 (J and K–K"). The GFP signal is not present when fused C-terminally to Pyr (I–I") but is present when inserted in frame within the predicted intracellular domain (K–K"). Scale bar, (I–I" and K–K") 10 μm.
See also Figures S2 and S3.

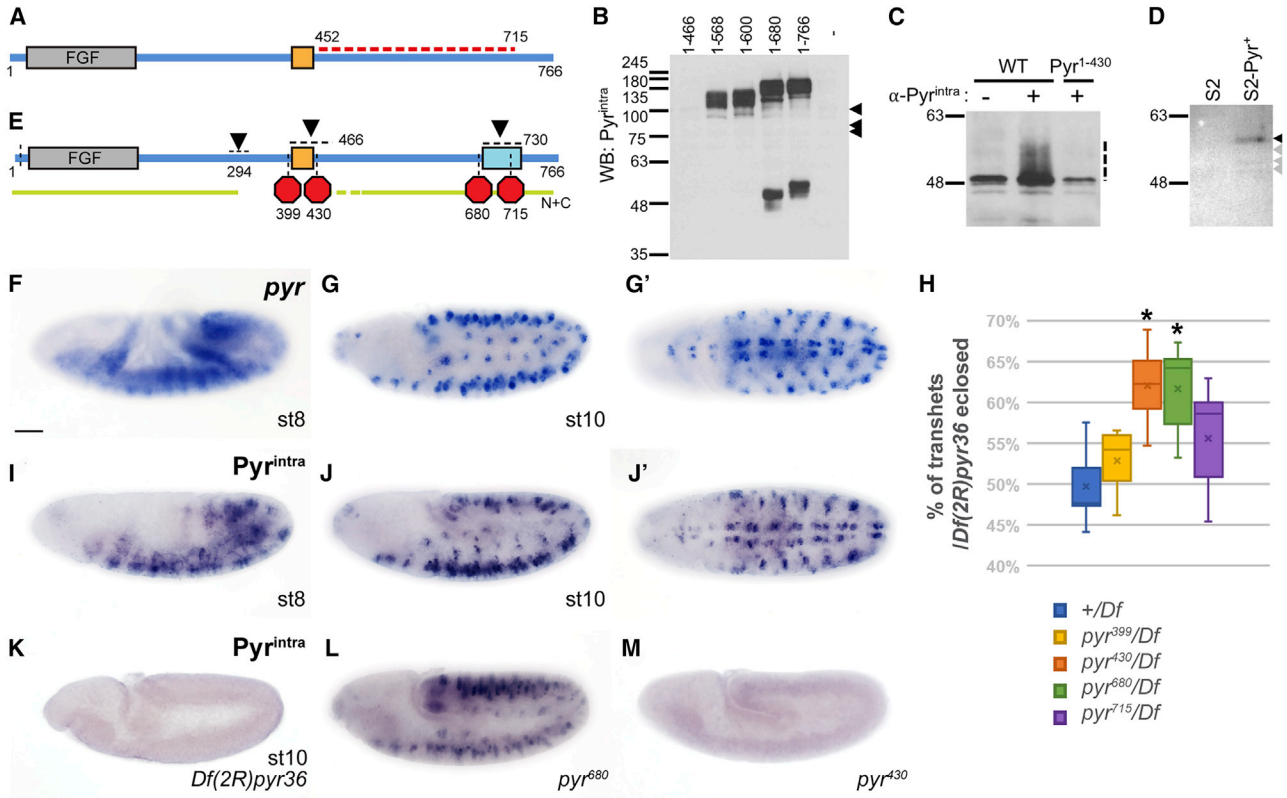

Figure 3. The C-Terminal Half of Pyr Is Intracellular and Is Spatiotemporally Regulated during Development

(A) Schematic of Pyr protein showing domain used to generate Pyr^{intra} antibody (dashed red line).

(B) Western blot of cell extracts (same used in Figure 1D) from transfected S2 cells expressing Pyr truncations, assayed using guinea pig anti-Pyr^{intra}, identify higher molecular weight (MW) Pyr^{intra} fragments that are likely full length, with corresponding RFP signals (Figures S1C and S1D), and lower MW bands separated from the N-terminal fragment. Arrowheads indicate the relative positions of 6xHis+mCh N-terminal fragments cleaved from Pyr^{intra} (Figures S1C and S1D). See Figure S1F for longer exposure.

(C and D) Immunoprecipitations and western blots from 3- to 7-h embryos (C) and S2 cells constitutively expressing 6xHis+mCh < Pyr1–766 > −3xFLAG. The prominent band at 48 kDa is non-specific, likely the abundant major yolk protein of 47–49 kDa [55, 56]. Dashed line indicates the molecular weight range of Pyr^{intra} IP material. For (D), IP from plain S2 cells is used as a negative control. A prominent band of ~57 kDa (black arrowhead) and minor bands (gray arrowheads) are seen.

(E) Sites of the *pyr* CRISPR-Cas9 mutants created in the course of this study.

(F–G' and I–J') Expression of Pyr in gastrulating (stage 8/st8) and stage 10 embryos. Pyr expression shown by immunostaining with anti-Pyr^{intra} antibody (I–J') closely tracks its mRNA localization detected by *in situ* hybridization using *pyr* riboprobe (F–G').

(H) Dosage of Pyr impacts the survival rate. Indicated *pyr* mutants were crossed to *Df(2R)pyr36/CyO* and the number of *pyr/Df* flies eclosed presented as percentage of total (>180 per cross). *pyr*^{430} and *pyr*^{680} alleles exhibit survival advantages over the wild-type allele ($n \geq 6$; $p < 0.005$).

(K–M) Pyr^{intra} immunostaining at stage 10. Pyr^{intra} signal is enhanced in *pyr*^{680} mutant embryos (L), whereas it is absent from *Df(2R)pyr36* and *pyr*^{430} mutant embryos (K and M), demonstrating the specificity of the antibody.

Embryos are shown with anterior to the left. Scale bar, 20 μm. See also Figure S1.

Collectively, these findings demonstrate these truncations (i.e., *pyr*^{430} and *pyr*^{680}) retain some function(s) and support the view that the TMD is a critical component of Pyr function.

The Pyr TMD and Degron Contribute to Localization of Htl Receptor and Protrusion Formation during Mesoderm Migration

Activation of Htl by Pyr and Ths triggers cell shape changes in the mesoderm, initiating a slow epithelial to mesenchymal transition (EMT) that continues as mesoderm cells spread upon the *pyr*-expressing ectoderm [9, 18, 19]. Htl is membrane associated and becomes concentrated at the tissue interface (arrowheads; Figures 4A, 4B', and 4C') [18, 20]. We hypothesized that localized expression of Pyr, possibly supported by its TMD, may be required for the concentration of Htl receptor.

We first investigated how Pyr expression changes over time. No antibody is available for direct localization of the Pyr extracellular region that contains the core FGF domain; however, anti-Pyr^{intra} is expected to recognize the full-length protein prior to the proteolytic cleavage that separates the extracellular portion from the TMD and C-terminal Pyr^{intra}. Therefore, Pyr^{intra} antibody was used as the best available proxy for full-length protein. Depending on developmental stages and cell types, Pyr localizes to both the cytoplasm and the membrane (Figures 4A–4D'). Specifically, until stage 9, Pyr is detected only within the cytoplasm in the neuroectoderm (Figures 4A–4C'). Later, during neurogenesis,

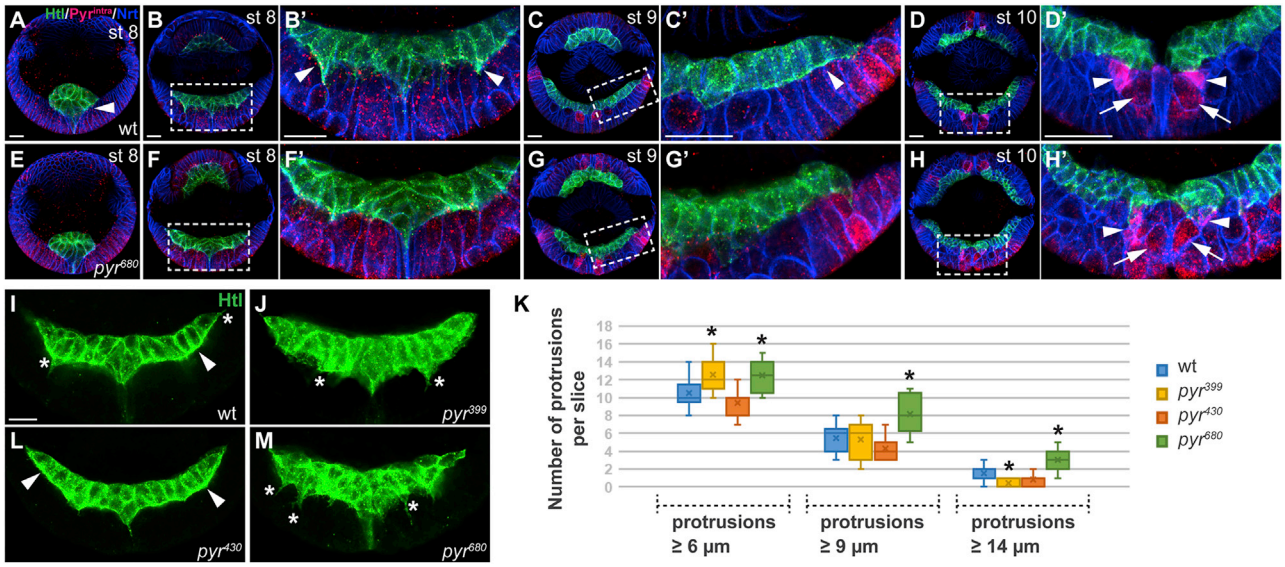

Figure 4. The C-Terminal Degron Regulates Pyr Expression in the Ectoderm and the Protrusive Activity of the Mesoderm, and the TMD Is Required for Enriching Htl at the Interface

(A–H'') Transverse cross sections (view of all *in vivo* immunostaining in current and subsequent figures unless otherwise noted) of stage 8 (A–B' and E–F'), stage 9 (C, C', G, and G'), and stage 10 (D, D', H, and H') wild-type or pyr^{680} mutant embryos co-stained with anti-Pyr^{intra} (pink), anti-Htl (labels mesoderm cells, green), and anti-Neurotactin (Nrt) (labels the basolateral cell membrane, blue) antibodies. Magnified views of the boxed areas are shown in panels to the right. Arrowheads and arrows indicate GMCs and NBs, respectively.

(I–M) Protrusive activity of mesoderm cells in stage 8 wild-type and indicated *pyr* mutant embryos was examined by Htl antibody staining (I, J, L, and M). Asterisks and arrowheads indicate mesoderm cell protrusions and enrichment of Htl at the meso-ecto interface, respectively. Numbers of protrusions are quantified in (K), which indicates that longer protrusions are formed in pyr^{680} mutants ($n \geq 7$; $p < 0.05$).

Scale bar, 20 μm. See also Video S1.

when neuroblasts (NBs) divide and give rise to ganglion mother cells (GMCs) and neurons [21], Pyr accumulates at the membrane of GMCs while being downregulated in NBs in stage 10 embryos (Figures 4D and 4D'; Video S1). This membrane staining likely indicates the presence of full-length protein or at minimum Pyr^{intra} with the TMD. Homozygous pyr^{680} mutants show similar staining patterns (Figures 4E–4H'), albeit at higher levels: the broad Pyr^{intra} staining at stage 8 is more visible in these mutants (Figures 4E and 4F' compared to Figures 4A and 4B'). At stage 10, when Pyr expression is restricted to the ventral midline neuronal lineage and the dorsal ectoderm region in wild-type embryos, ectopic anti-Pyr^{intra} signals are observed in pyr^{680} mutants (Figure 4H). These results are consistent with the idea that the Pyr C-terminal degron functions to fine-tune the temporal expression domains of the ligand *in vivo* while also pointing to a potential role for the degron in the support of neuronal patterning.

Pyr engages Htl at the basal membrane of migrating mesoderm cells, where both radial (into ectoderm) and dorsal protrusions are observed [22]. Directional protrusion formation largely depends on the activation of Htl by Pyr, acting upstream of Rho family guanosine triphosphatases (GTPases) [8, 9, 19, 23]. To investigate how the Pyr TMD and/or the degron might function to support FGF forward signaling, we examined the phenotypes of *pyr* truncation mutants utilizing Htl antibody staining, which clearly illuminates cell membranes and protrusions of the mesoderm.

Mesoderm cells in wild-type embryos exhibit localized long protrusions at stage 8 (asterisk, Figure 4I), with concentrated Htl at the basal interface (arrowhead, Figure 4I). Dorsal-directed protrusions, induced by Rac GTPases [24], appear largely normal in *pyr* truncation mutants. When the entire C terminus is removed in pyr^{430} mutants, Htl is visibly further enriched at the interface (arrowheads, Figure 4L), although the number of mesoderm protrusions remains largely unchanged (Figure 4K). In pyr^{399} mutants lacking both the TMD and C terminus, Htl seems less enriched where smaller radial protrusions (<9 μm) increase in number and occasionally bifurcate (asterisks, Figures 4J and 4K). Remarkably, upon removal of the degron, mesoderm cells in pyr^{680} mutants become extremely protrusive, extending long projections into the ectoderm that also branch out extensively (asterisks, Figures 4K, 4M, and S4F). In contrast to dorsal-directed protrusion, formation of these radially directed finger-like membrane extensions is driven by actin nucleators under the control of another small GTPase, Cdc42 [9]. Together, our results suggest that the Pyr TMD facilitates the enrichment of Htl and limits the number of protrusions at the basal side of the mesoderm; although the C-terminal degron, by controlling levels and distribution of Pyr, influences length, number, and morphology of those protrusions, possibly through regulating Cdc42 activity (see Discussion).

The Pyr TMD and Degron Contribute to the Strength and Spatial Precision of MAPK Signaling

Immunostaining reveals that 1∼2 mesoderm cells at the dorsal-most position are positive for di-phosphorylated Erk (dpERK) on each side of the migrating mesodermal collective

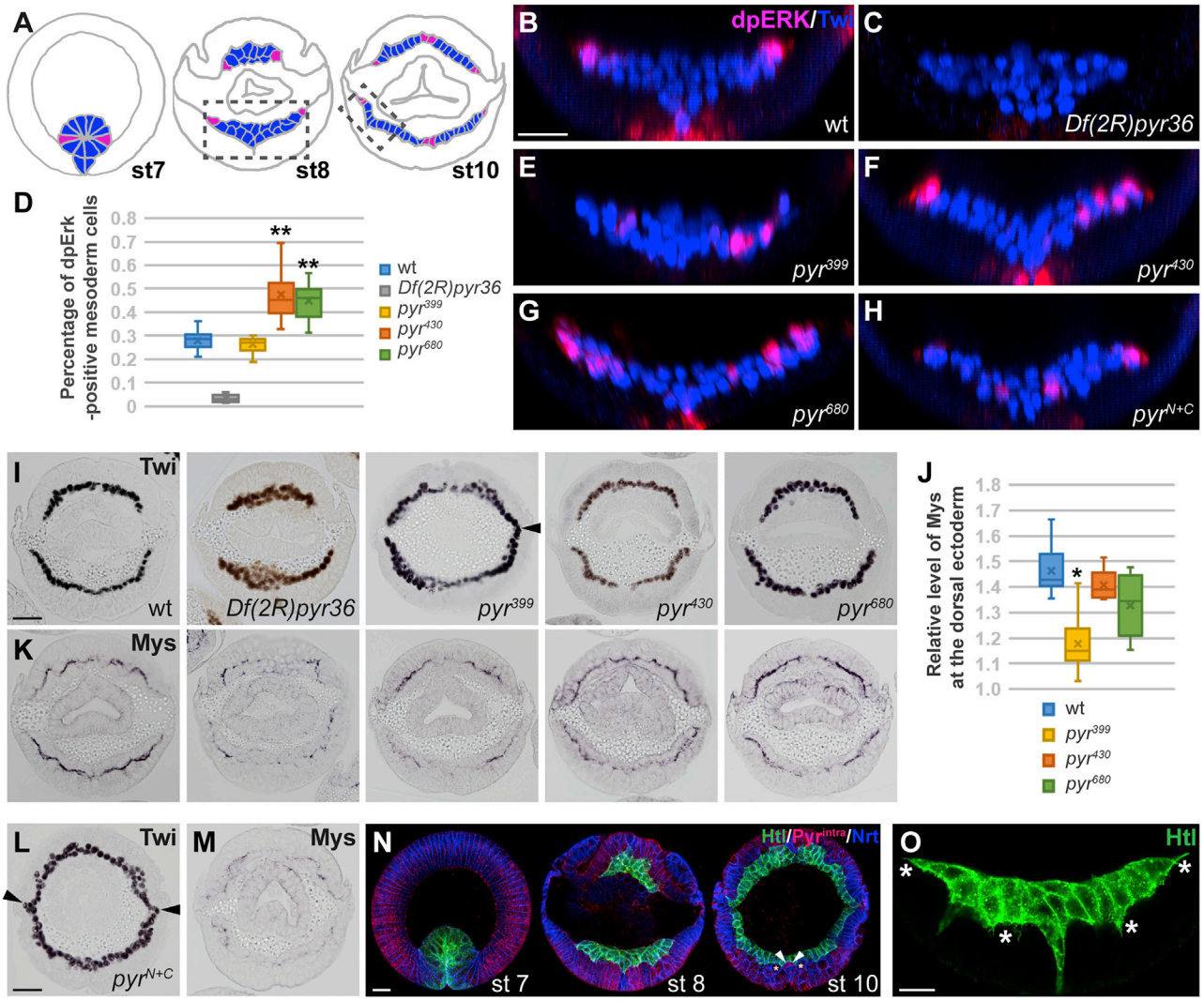

Figure 5. Differential Requirement for Pyr TMD and C-Terminal Degron during Multi-step Mesoderm Development

(A) Diagram of transverse sections of stage 7–10 wild-type embryos, highlighting activation of ERK (pink) in mesoderm cells (blue) during mesoderm spreading.

(B, C, and E–H) Images relate to boxed area of stage 8 embryos in schematic in (A) showing embryos co-stained with anti-dpErk (pink) to detect MAPK signaling pathway activation and anti-Twist (Twi) to identify mesoderm cells (blue). Enriched dpERK at the leading front of migrating mesoderm cells in the wild-type (B) is lost in *pyr*-null mutant (C), reduced in pyr^{399} and pyr^{N+C} mutants (E and H), while expanded to ectopic cells within pyr^{430} and pyr^{680} mutants (F and G). *Z* projections of confocal images are shown, obtained by scanning embryos from the ventral side.

(D) Statistical analysis of percentage of dpERK+ mesoderm cells in stage 8 embryos as in (B, C, and E–G). Both pyr^{430} and pyr^{680} embryos contain significantly more dpErk-positive mesoderm cells compared to the wild-type ($n \geq 6$; $p < 0.0001$; STAR Methods).

(I and K) Stage 10 embryos stained by either anti-Twi (I) or anti-Mys (K) antibodies showing the mesoderm spreading phenotypes, including non-monolayer formation and lack of uniform expression of Mys at mesoderm-ectoderm boundary, for indicated genotypes.

(J) Quantification of relative Mys levels at the dorsal ectoderm-mesoderm interface (STAR Methods). Region of interest is illustrated as the boxed area in stage 10 embryo in (A). Levels in pyr^{399} mutants are significantly lower than wild-type or pyr^{430} embryos ($n = 8$; $p < 0.0005$).

(L and M) Stage 10 pyr^{N+C} mutant embryos stained by anti-Twi (L) and anti-Mys (M) antibodies. The mesoderm cells, marked by Twi (L), form a complete circle and exhibit reduced levels of Mys (M) compared to (K).

(N) Stage 7, 8, and 10 pyr^{N+C} mutant embryos co-stained with anti-Pyr^{intra} (pink), anti-Htl (green), and anti-Nrt (blue) antibodies.

(O) Stage 8 pyr^{N+C} mutants stained with anti-Htl antibody. Asterisks indicate mesoderm cell protrusions.

Scale bar, 20 μm. See also Figure S4.

in wild-type embryos at late stage 8 (Figures 5A and 5B) [25]. This pattern is completely lost when the *pyr* gene is deleted in entirety (i.e., *Df(2R)pyr36*; Figure 5C), demonstrating a requirement for *pyr* in Htl-dependent mitogen-activated protein kinase (MAPK) signaling activation, which is consistent with previous studies [8, 9, 26]. In pyr^{399} mutants, there is either a weak, variable loss of dpERK signal at the leading edge or delocalized signal within the mesoderm (Figure 5E). In contrast, pyr^{430} and pyr^{680} mutants exhibit ectopic dpERK staining in addition to that in the dorsal leader cells (Figures

5F and 5G). Both mutants show a significant increase in the percentage of dpERK+ mesoderm cells compared to the wild type during migration (Figure 5D), suggesting that removal of the C-terminal degron while leaving the TMD intact results in an increase in levels of localized Pyr presented by the ectoderm and ectopic MAPK signaling activation in the mesoderm.

Pyr TMD Plays a Major Role in Mesoderm Migration and Polarity Formation

Though mesoderm cells do not require FGF signaling to move, as spreading still occurs in mutants deficient in either the receptor or ligands [8, 27], monolayer formation is indeed FGF dependent and essentially involves a mesenchymal to epithelial transition (MET) that takes place at the end of migration [18]. This event is marked by the polarized localization of β-integrin, myospheroid (Mys), at the basal interface between the mesoderm and ectoderm at stage 10 [8, 28]. Disrupting polarity formation in the mesoderm leads to uneven spreading, which affects differentiation of the muscle precursor cells at a later developmental stage [18, 29].

Despite the presence of ectopic dpERK+ mesoderm cells in pyr^{430} and pyr^{680} mutants, embryos of each genotype go on to form a largely normal monolayer at stage 10, as examined by Twist (Twi) antibody staining (Figure 5I). However, embryos homozygous for pyr^{399} exhibit a striking phenotype that, to our knowledge, has not been documented previously. Mesoderm cells clearly over-migrate in 20% of pyr^{399} embryos examined: Twi+ cells from the bottom half connect with those ones from the top (arrowhead, Figure 5I). These results suggest that the Pyr TMD is required for mesoderm cells to halt movement beyond the dorsal ectoderm domain, possibly by affecting cell-cell adhesion and/or by inducing cells to acquire polarity. Indeed, the level of Mys at the dorsal mesoderm-ectoderm interface is significantly lower in homozygous pyr^{399} mutants or $pyr^{399}/Df(2R)pyr36$ transheterozygotes, although it is not changed in pyr^{430} mutants compared to wild type (Figures 5J, 5K, and S6A–S6E), indicating a requirement for the TMD in establishing proper cell polarity and regulation of the extent of cell migration.

To directly investigate the critical requirement for the Pyr TMD in supporting FGF forward signaling associated with the N-terminal extracellular domain, another allele, pyr^{N+C}, was generated, essentially representing a version of Pyr in which the N-terminal fragment is disconnected from the TMD and the intracellular region (green line, Figure 3E; STAR Methods). In approximately 50% of pyr^{N+C} mutants, mesoderm cells migrate further, to the dorsal-most position of the ectoderm. Due to germ-band extension (GBE), it appears as a full circle in cross sections at stage 10 (arrowheads, Figure 5L) and also is accompanied by a further reduction in Mys expression relative to pyr^{399} mutants (Figure 5M). Similar to pyr^{399}, dpERK staining in the mesoderm appears reduced or delocalized (Figure 5H), and significantly more protrusions are observed (asterisks, Figures 5O and S4G). As the Pyr intracellular domain is expressed (Figure 5N), these defects demonstrate that proper function of the Pyr N-terminal FGF domain requires its linkage to the TMD to regulate MAPK signaling and protrusion formation.

The Degron Is Required for Pyr Apical Enrichment and Proper Localization of Cell Polarity Regulators in the Blastoderm Embryo

At stage 6, we found that, in contrast to the uniform localization of *pyr* mRNA (Figures 6A and 6A'), Pyr protein is enriched apically in lateral regions of the embryo, within the presumptive neuroectoderm (Figures 6D and 6D'). Also consistent with our cell culture results, levels of Pyr^{intra} increase by approximately 20% in pyr^{715} mutants and 30% in pyr^{680} mutants compared to the wild type (Figures 6B and 6E), indicating that the C-terminal degron (i.e., aa 681–766) functions *in vivo* to control Pyr^{intra} protein levels (Figure 2D). Surprisingly, those embryos also show readily apparent basal Pyr^{intra} localization (Figure 6B), suggesting that the degron also influences the intracellular distribution of Pyr^{intra} as an independent fragment and as a part of other Pyr isoforms prior to proteolytic cleavage around the TMD. Perhaps as a result of this ectopic localization, both pyr^{680} and pyr^{715} mutants exhibit varying degrees of mesoderm invagination defects, among which a two-centered furrow was observed in about 10% of embryos examined (Figures 6C and 6F).

Invagination is driven by factors controlling actomyosin contraction within the presumptive mesoderm [30], although coordinated cell shape changes of neighboring ectoderm cells are necessary for the correct timing of this process [31]. Adherens junctions (AJs) function to integrate the mechanical forces across the cortical cell membrane, ensuring the fidelity of this critical morphogenetic movement [32, 33]. To better understand the cause of invagination defects in *pyr* mutants, we examined the localization of β-catenin (Armadillo in *Drosophila* [Arm]), a key component of AJs. Mutants expressing higher levels of Pyr^{intra}, either resulting from modification of *pyr* sequence (i.e., pyr^{680} and pyr^{N+C}) or ectopic expression of the C-terminal fragment (aa 431–766) or full-length protein via ubiquitous maternal *tub>GAL4* driver [34], exhibit increases in levels of Arm associated with basal AJs (asterisks, Figures 6G–6L and 6N). In contrast, Arm localization appears normal in mutants overexpressing the N-terminal fragment (upstream activating sequence [UAS]-PyrNterm; aa 1–466) [5] or loss of Pyr^{intra} (Figures 6K and 6M). These data further support the view that mistargeting of Arm to basal regions in epithelial cells depends on the action of Pyr^{intra}, possibly linked to the defective invagination observed in *pyr* mutants lacking the degron.

Normally apically enriched, Pyr^{intra} is ectopically localized to the basal side of ectoderm cells in lateral regions of pyr^{680}, pyr^{715}, and pyr^{N+C} mutants while also present at higher levels. However, mislocalized Arm extends throughout the embryo in these mutants, not limited to Pyr-expressing cells, suggesting this phenotype is an indirect effect. Therefore, we asked whether other cell polarity regulators that usually act upstream of or in parallel with AJs are affected locally.

Apicobasal polarity in the embryonic ectoderm is established during cellularization under the control of a series of conserved apical polarity regulators [35–37]. *crumbs* (*crb*) encodes a transmembrane protein that marks the apical membrane domain in epithelial cells [38]. The homolog of mammalian Par3, Bazooka (Baz), is situated beneath Crb and co-localizes with the cadherin-catenin complexes at the apical AJs [39]. The expression pattern of Crb is largely maintained in these *pyr* mutants (i.e., pyr^{680}, pyr^{715}, and pyr^{N+C}). However, localization of Baz at the

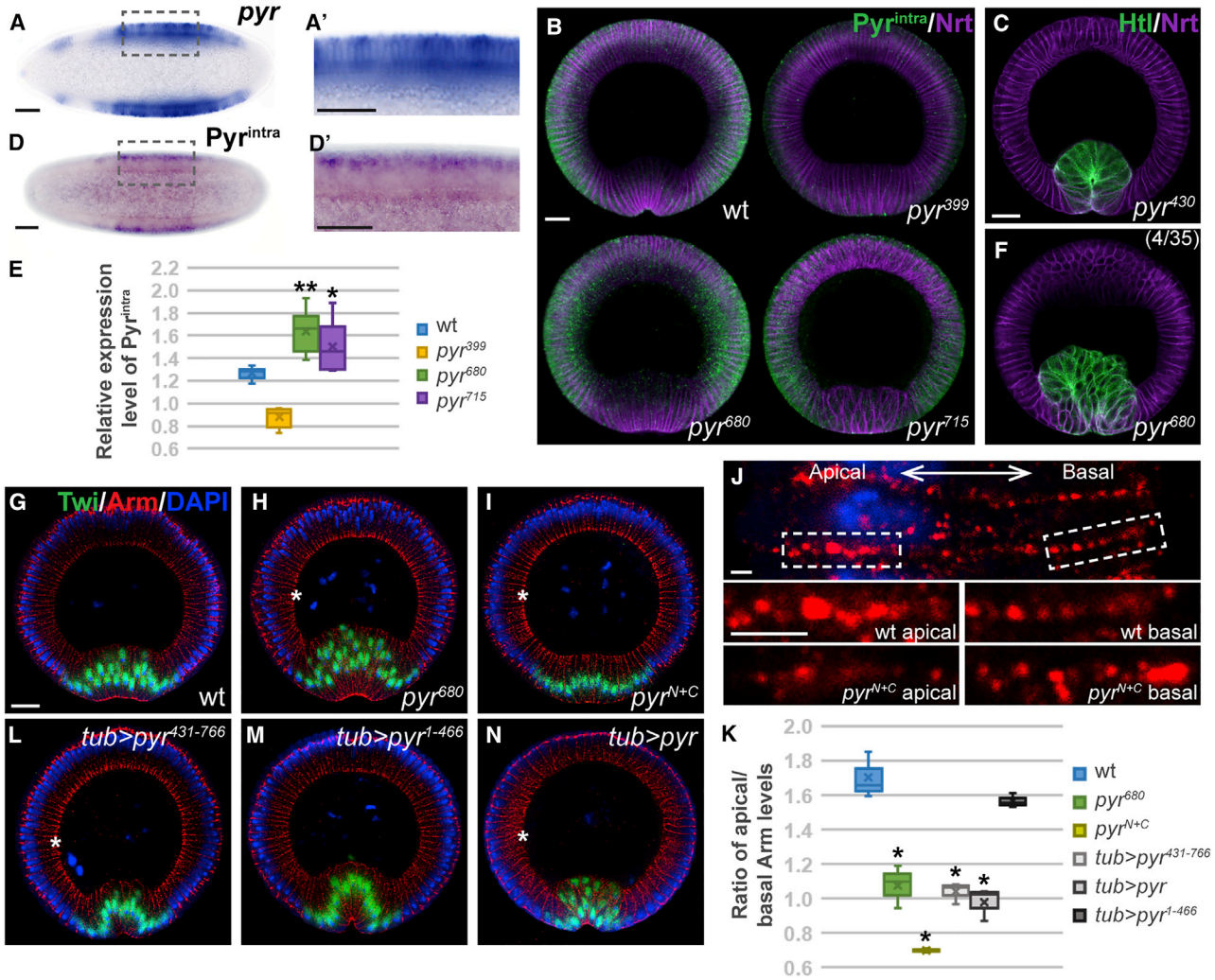

Figure 6. The Pyr C Terminus Regulates Its Expression Levels and Influences Apicobasal Polarity of Cells, *In Vivo* and *In Vitro*

(A, A', D, and D') Whole-mount *in situ* hybridization using riboprobe to *pyr* (A) in comparison to immunostaining using anti-Pyr^{intra} (D). Ventral views of stage 6 embryos are shown, with anterior to the left. Magnified views of boxed areas in (A) and (D) shown in (A') and (D'), respectively.

(B) Stage 6 embryos co-stained by anti-Pyr^{intra} (green) and anti-Nrt (purple) to show cell outlines.

(E) Quantification of immunofluorescence staining for images in (B) (STAR Methods). Both *pyr*^{680} and *pyr*^{715} mutants exhibit a significantly higher (~25%) level of Pyr^{intra} expression ($n \geq 6$; $p < 0.005$ and $p < 0.05$, respectively).

(C and F) Stage 7 mutant embryos stained with anti-Htl (green) and anti-Nrt (purple) showing a severe phenotype of a double invaginated tube associated with *pyr*^{680} (F; n = 4/35) in comparison to wild-type or *pyr*^{430} in which only a single invaginated tube forms (C).

(G–I and L–N) Stage 6 embryos of indicated genotypes co-stained by anti-Arm (red), anti-Twi (green; marks the mesoderm cells), and DAPI (blue; marks nuclei). Asterisks indicate possible increased levels of Arm detected in the basal regions of epithelial cells of indicated mutants (H, I, L, and N) compared to wild-type (G), while distribution of Arm is unchanged in *tub>pyr*$^{1-466}$ (M). Twi (green) antibody marks mesoderm cells, and DAPI (blue) labels nuclei.

(J and K) Ratios of apical versus basal Arm levels (J, magnified view of areas in G and I) were calculated (K) and demonstrate mislocalized Arm is associated with *pyr*^{680}, *pyr*$^{N+C}$, *tub > pyr*$^{431–766}$, and *tub>pyr* mutants (n = 3; $p < 0.005$; STAR Methods), but not *tub > pyr*$^{1–466}$, which is similar to wild type. Scale bar, (J) 2 μm. Scale bar, 20 μm (except for J). See also Figure S5.

cortical membrane extends basally in the presumptive neuroectoderm region, where Pyr^{intra} is locally present at higher levels (arrowheads, Figures 7B and 7C). When Pyr^{intra} or Pyr is ubiquitously expressed driven by *tub>GAL4*, mislocalization of Baz is observed throughout the entire embryonic ectoderm (Figures 7E', 7G, and S6B'). The correlation between levels of Pyr^{intra} and its local effect on Baz localization is most apparent in *pyr*$^{N+C}$ mutants: basally extended Baz patterns are associated with elevated endogenous Pyr^{intra} levels in the lateral regions (Figure 7C), although in the dorsal ectoderm that does not express Pyr, Baz remains apically localized (Figure S6A'). In contrast, overexpression of the Pyr N-terminal fragment [5] or full-length Ths (UAS-Ths) [4] has no effect on Baz (Figures 7F, S6F, and S6F') and neither does loss of Pyr^{intra} (i.e., *pyr*^{399}, *pyr*^{430}, and *Df(2R)pyr36*; Figures S6C–S6E'). These results collectively suggest that dysregulation of Pyr^{intra} (i.e., high levels) affects local apicobasal cell polarity, supporting a cell-autonomous role for Pyr^{intra}.

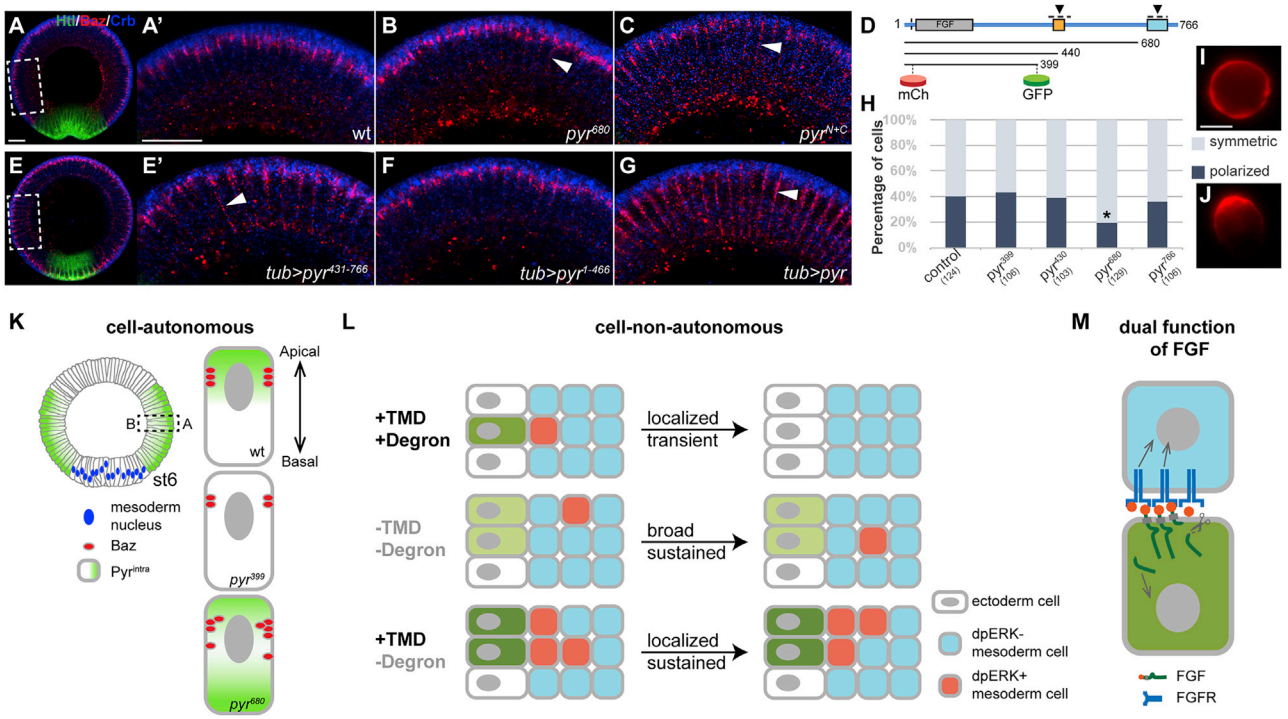

Figure 7. Utilization of TMD, Degron, or Cleavage Allows Flexibility in the Regulation of FGF Signaling

(A–C and E–G) Lateral regions of stage 6 embryos stained with Baz (red) and Crb (blue). Whole-embryo views (A and E) are labeled with anti-Htl (green) to show mesoderm cell morphology and location of boxed areas with magnified views in (A') and (E'). Baz is concentrated at the apical AJ regions beneath Crb-positive domains in wild-type (A') and *tub>pyr*$^{1-466}$ (F) embryos, while its membrane localization extends basally in *pyr*^{680} (B) and *pyr*$^{N+C}$ (C) mutants or upon ubiquitous ectopic expression of the C-terminal fragment (E') or full-length Pyr (G), indicated by arrowheads. Scale bar, 20 μm.

(D) Schematic of dual-tagged Pyr constructs used in assays of S2 cell polarity.

(H–J) Graph depicting percentages of S2 cells (H) exhibiting one of two possible Baz-mKate localizations: symmetric (I) or polarized (J) upon co-expression of Baz-mKate with the indicated Pyr constructs. Asterisk indicates statistical significance reached by chi-square test; $p < 0.001$. Scale bar, 10 μm.

(K–M) Models for the dual function of Pyr. A cell-autonomous role for Pyr in regulating apicobasal polarity of epithelial cells is shown, as manifested by the localization of Baz in lateral regions of the embryo where *pyr* is expressed (green; K). Utilization of the TMD and degron enables precisely regulated spatiotemporal outputs for Pyr in signaling to Htl-expressing cells (blue), resulting in activation of the intracellular MAPK pathway (red), and loss of one and/or the other through proteolysis can modulate signaling outputs, which may be advantageous for different developmental roles (L). FGFs may function bidirectionally (M). See also Figures S5 and S6.

To provide further evidence, we performed a cell-based polarity assay, utilizing the cultured S2 cells, which in their naive state do not express Htl or display intrinsic asymmetry [40, 41]. Overexpression of Baz induces a process of apicobasal polarity formation, which is monitored through tagging Baz with a fluorophore [41]. Constructs expressing truncated Pyr proteins analogous to the CRISPR-derived *pyr* mutants were co-expressed with Baz, and their effects on polarity formation were documented 72 h post-transfection (Figure 7D). In the control experiment, ~40% polarize and ~60% of cells remain symmetric, as determined by Baz-mKate localization (Figures 7H–7J). Co-expression of Pyr 1–399, 1–430, or 1–766 do not change this rate. However, when Pyr 1–680 is co-transfected with Baz, the percentage of polarized S2 cells drops to 19% (asterisk, Figure 7H), consistent with our *in vivo* results that markers for apicobasal polarity are mislocalized in *pyr*^{680} mutants and collectively support a role for Pyr^{intra} in regulating cell polarity. Surprisingly, co-transfection of full-length Pyr (i.e., 1–766) in S2 cells fails to diminish the induced asymmetry (Figure 7H). It is possible that, when polarity is induced in S2 cells, Baz is overexpressed to such a high level that full-length Pyr is insufficient to interfere with its function.

DISCUSSION

Our data suggest that the TMD and degron, two regulatory domains in the *Drosophila* FGF Pyr that have not been previously identified in any FGF, provide precision and fidelity to Pyr functions: its cell non-autonomous role in Htl-dependent MAPK signaling (Figure 5) as well as a novel cell-autonomous role in supporting apicobasal polarity (Figure 6). Expressing Pyr in a purely secreted form (i.e., lacking the TMD and intracellular portions or disconnecting the TMD from the extracellular domain) causes delocalized MAPK activation *in vivo*, suggesting that, to achieve signaling precision/optimal outputs, functions of the TMD and N-terminal extracellular domain are coordinated to delay or limit the diffusion of secreted Pyr from its source (Figure 7L, middle panel versus top panel). Removing the degron causes gain-of-function phenotypes, including the activation of MAPK signaling in a broader spatial domain that perdures inappropriately

(Figure 7L, bottom versus top panel), suggesting it not only limits the strength and duration of cell non-autonomous forward signaling (mediated by extracellular FGF domain and TMD through Htl) but also regulates cell-autonomous responses (supported by intracellular, extended C-terminal sequence; Figures 7K and 7M).

One of the most intriguing mutant phenotypes identified is the over-migration of mesoderm cells. In embryos homozygous for pyr^{N+C} and pyr^{399} alleles (arrowhead, Figures 5I and 5L), mesoderm cells send out smaller, delocalized protrusions, suggesting that the receptor-ligand interaction is suboptimal (Figures 4I and 5O), which perhaps leads to less-efficient Mys enrichment at the mesoderm-ectoderm interface (Figures 5J, 5K, and 5M) and a failed MET. We postulate that not only is MET crucial for downstream differentiation events but also that it functions to prevent mesoderm cells from moving beyond their normal dorsal ectoderm stopping point. Therefore, removing or disconnecting the TMD from the N-terminal FGF domain compromises the brake on migration (i.e., Mys) and allows mesoderm cells to retain mobility longer than they should.

Migrating mesoderm cells in pyr^{680} mutants also project longer and more branched protrusions at the basal plasma membrane, indicative of increased activity in actin polymerization downstream of Cdc42 [9, 24]. Cdc42 functions to stimulate actin nucleation and polymerization through either the formin Diaphanous (Dia) or Wiskott-Aldrich syndrome protein (WASp). Though the exact mechanism by which Pyr regulates Cdc42 activity remains elusive, it may involve utilization of WASp-dependent actin nucleation, as extensive protrusion branching is observed in pyr^{680} mutants. Therefore, forward FGF signaling active within mesoderm cells regulates both protrusion formation (Figures 4I–4M) as well as integrin-based adhesion (Figure 5K), and both of these cellular processes respond to levels and distribution of Pyr presented by the ectoderm.

This study identifies Pyr as a type I membrane protein, the first FGF protein identified with this topology, with an extended C-terminal intracellular domain and presents compelling evidence for its function in regulating apicobasal cell polarity, potentially through a reverse signaling mechanism, which remains an important area of future experimentation. Interactions between Pyr^{intra} and cytoplasmic proteins, such as cytoskeletal components or other intracellular-acting proteins, may impact cell polarity. It is also possible that Pyr or Pyr^{intra}, when accumulated to high levels (i.e., in pyr^{680} mutants), act in a dominant-negative fashion and hijack or redirect the secretory pathways of other proteins, including Baz.

We propose that spatiotemporally refined activity of (yet unknown) proteases normally shapes Pyr function to diversify its range and signal strength through alternative usage of the TMD and degron, depending on which of the cleavage sites are utilized (see Figure S1). Alternative cleavage could therefore enable differential activity of the N-terminal FGF domain and perhaps also Pyr^{intra} separated from the rest of the molecule. Besides controlling its stability, alternative cleavage and removal of the degron is likely influencing the subcellular localization of Pyr^{intra}. We hypothesize that the apically enriched localization of Pyr^{intra} in the presumptive ectoderm at the lateral sides of the blastoderm embryo results from alternative removal of the degron apically, but not basally, possibly by polarized protein trafficking and/or degradation.

The utilization of a TMD and degron in Pyr activity may indicate functional conservation of more ancestral yet general properties critical to the regulation of FGF signaling. These include the range of the FGF molecule and the intensity and duration of its signal receiving cells, in order to expand the signaling palette of a single ligand-receptor pair. Some of these properties may be maintained through utilization of domains identical to those found in Pyr; for example, we have also found that one isoform of another *Drosophila* FGF, Bnl, contains a previously uncharacterized C-terminal TMD (Figure S5) that could affect the levels and distribution of Bnl available for access by the cytoneme-bound receptor, Breathless [42, 43], in coordination with the proteolytic cleavage already known to regulate Bnl distribution [44]. Conditional utilization of functional domains outside of the FGF homologous portions in FGFs, such as the TMD and degron of Pyr, is likely to regulate spatiotemporal dynamics and availability of many FGFs as ligands. In vertebrates, FGF21 and FGF23 have been shown to differentially interact with FGF receptor (FGFR)/co-receptor (Klotho) complexes, depending on their cleavage state [45–47].

Not all FGFs are secreted via a canonical signal-peptide or bind receptors to enact signaling, and the potential function(s) and regulation of these pools of proteins are relatively unstudied. FGF11/12/13/14 family members remain intracellular and function as cofactors in voltage-gated sodium channels, and bipartite nuclear localization sequences in the N termini of each direct their localization to the nucleus [48]. Nuclear localization is also observed for specific isoforms of vertebrate FGF1, FGF2, and FGF3, as well as *C. elegans* LET-756 [49, 50]. Like Pyr, LET-756 has an extended C-terminal domain, and a mutation that leaves its FGF domain intact while truncating ~100 aa from its C terminus results in deficiencies in growth and development [51]. These studies, and our data demonstrating a cell-autonomous role for Pyr, indicate that assorted FGF functions are possible. Though domains such as TMDs and degrons may not be utilized broadly across the evolutionarily diverse FGF protein family, it is likely that many of their activities and regulatory elements are functionally conserved and have adapted to serve the functional needs of particular organisms.

STAR★METHODS

Detailed methods are provided in the online version of this paper and include the following:

- KEY RESOURCES TABLE
- RESOURCE AVAILABILITY
  - Lead Contact
  - Materials Availability
  - Data and Code Availability
- EXPERIMENTAL MODEL AND SUBJECT DETAILS
  - Transgenic flies and CRISPR/Cas9 mutagenesis
  - Fly stocks and survival assay
  - Cell culture
- METHOD DETAILS
  - Plasmids and clones
  - Pulldown of FGFs from cell culture supernatants
  - Generation of anti-Pyr^{intra} antibodies
  - Immunoprecipitation

- Whole mount *in situ* hybridization, immunohistochemistry and immunofluorescence
- Plastic sectioning of embryos, and imaging fluorescent signals
- S2 cell assay of Baz polarization
- Tethering of mCh-Pyr to the plasma membrane with TMDs

- QUANTIFICATION AND STATISTICAL ANALYSIS
  - Secondary structure prediction and multiple sequence alignments of Pyr
  - Quantification of the mesoderm protrusions, dpERK positive cells and immunofluorescence of Mys, Pyr^{intra} and Arm

SUPPLEMENTAL INFORMATION

Supplemental Information can be found online at https://doi.org/10.1016/j.cub.2020.06.006.

ACKNOWLEDGMENTS

We thank Fumio Matsuzaki, David Kosman, and Jennifer Zallen for providing constructs or antibodies and Frank Macabenta and Kai Zinn for comments on the manuscript. This study was supported by grants R35GM118146 from the National Institute of General Medical Sciences (NIGMS) to A.S., PF-15-202-01-DDC from the American Cancer Society to V.S., and the Chen Director's Award from the Tianqiao and Chrissy Chen Institute for Neuroscience to A.S.

AUTHOR CONTRIBUTIONS

A.S., V.S., and J.S. conceived the project and planned the experimental approach. A.S. directed the project. V.S. performed all protein and cell culture studies and bioinformatic analysis of proteins and generated Pyr^{intra} antibodies and CRISPR-Cas9 mutants. J.S. performed all the stainings, quantitative analysis of imaging data, and viability studies. Data were analyzed by V.S., J.S., and A.S. The manuscript was written by V.S., J.S., and A.S.

DECLARATION OF INTERESTS

The authors declare no competing interests.

Received: March 17, 2020
Revised: May 13, 2020
Accepted: June 1, 2020
Published: July 2, 2020

REFERENCES

1. Ornitz, D.M., and Itoh, N. (2015). The fibroblast growth factor signaling pathway. Wiley Interdiscip. Rev. Dev. Biol. *4*, 215–266.
2. Liu, Y., Ma, J., Beenken, A., Srinivasan, L., Eliseenkova, A.V., and Mohammadi, M. (2017). Regulation of receptor binding specificity of FGF9 by an autoinhibitory homodimerization. Structure *25*, 1325–1336.e3.
3. Rodriguez-Enfedaque, A., Bouleau, S., Laurent, M., Courtois, Y., Mignotte, B., Vayssière, J.-L., and Renaud, F. (2009). FGF1 nuclear translocation is required for both its neurotrophic activity and its p53-dependent apoptosis protection. Biochim. Biophys. Acta *1793*, 1719–1727.
4. Stathopoulos, A., Tam, B., Ronshaugen, M., Frasch, M., and Levine, M. (2004). pyramus and thisbe: FGF genes that pattern the mesoderm of Drosophila embryos. Genes Dev. *18*, 687–699.
5. Tulin, S., and Stathopoulos, A. (2010). Analysis of thisbe and pyramus functional domains reveals evidence for cleavage of Drosophila FGFs. BMC Dev. Biol. *10*, 83.
6. Gisselbrecht, S., Skeath, J.B., Doe, C.Q., and Michelson, A.M. (1996). heartless encodes a fibroblast growth factor receptor (DFR1/DFGF-R2) involved in the directional migration of early mesodermal cells in the Drosophila embryo. Genes Dev. *10*, 3003–3017.
7. Beiman, M., Shilo, B.Z., and Volk, T. (1996). Heartless, a Drosophila FGF receptor homolog, is essential for cell migration and establishment of several mesodermal lineages. Genes Dev. *10*, 2993–3002.
8. McMahon, A., Reeves, G.T., Supatto, W., and Stathopoulos, A. (2010). Mesoderm migration in Drosophila is a multi-step process requiring FGF signaling and integrin activity. Development *137*, 2167–2175.
9. Clark, I.B.N., Muha, V., Klingseisen, A., Leptin, M., and Müller, H.-A.J. (2011). Fibroblast growth factor signalling controls successive cell behaviours during mesoderm layer formation in Drosophila. Development *138*, 2705–2715.
10. Trisnadi, N., and Stathopoulos, A. (2014). Ectopic expression screen identifies genes affecting Drosophila mesoderm development including the HSPG Trol. G3 (Bethesda) *5*, 301–313.
11. Knox, J., Moyer, K., Yacoub, N., Soldaat, C., Komosa, M., Vassilieva, K., Wilk, R., Hu, J., Vazquez Paz, L.d.L., Syed, Q., et al. (2011). Syndecan contributes to heart cell specification and lumen formation during Drosophila cardiogenesis. Dev. Biol. *356*, 279–290.
12. Käll, L., Krogh, A., and Sonnhammer, E.L.L. (2007). Advantages of combined transmembrane topology and signal peptide prediction–the Phobius web server. Nucleic Acids Res. *35*, W429–W432.
13. Bogdanov, M., Dowhan, W., and Vitrac, H. (2014). Lipids and topological rules governing membrane protein assembly. Biochim. Biophys. Acta *1843*, 1475–1488.
14. Kuroiwa, T., Sakaguchi, M., Mihara, K., and Omura, T. (1990). Structural requirements for interruption of protein translocation across rough endoplasmic reticulum membrane. J. Biochem. *108*, 829–834.
15. Kadam, S., Ghosh, S., and Stathopoulos, A. (2012). Synchronous and symmetric migration of Drosophila caudal visceral mesoderm cells requires dual input by two FGF ligands. Development *139*, 699–708.
16. Port, F., Chen, H.-M., Lee, T., and Bullock, S.L. (2014). Optimized CRISPR/Cas tools for efficient germline and somatic genome engineering in Drosophila. Proc. Natl. Acad. Sci. USA *111*, E2967–E2976.
17. Kadam, S., McMahon, A., Tzou, P., and Stathopoulos, A. (2009). FGF ligands in Drosophila have distinct activities required to support cell migration and differentiation. Development *136*, 739–747.
18. Sun, J., and Stathopoulos, A. (2018). FGF controls epithelial-mesenchymal transitions during gastrulation by regulating cell division and apicobasal polarity. Development *145*, dev161927.
19. Wilson, R., Vogelsang, E., and Leptin, M. (2005). FGF signalling and the mechanism of mesoderm spreading in Drosophila embryos. Development *132*, 491–501.
20. Michelson, A.M., Gisselbrecht, S., Zhou, Y., Baek, K.H., and Buff, E.M. (1998). Dual functions of the heartless fibroblast growth factor receptor in development of the Drosophila embryonic mesoderm. Dev. Genet. *22*, 212–229.
21. Homem, C.C.F., and Knoblich, J.A. (2012). Drosophila neuroblasts: a model for stem cell biology. Development *139*, 4297–4310.
22. Gryzik, T., and Müller, H.-A.J. (2004). FGF8-like1 and FGF8-like2 encode putative ligands of the FGF receptor Htl and are required for mesoderm migration in the Drosophila gastrula. Curr. Biol. *14*, 659–667.
23. Schumacher, S., Gryzik, T., Tannebaum, S., and Müller, H.-A.J. (2004). The RhoGEF Pebble is required for cell shape changes during cell migration triggered by the Drosophila FGF receptor Heartless. Development *131*, 2631–2640.
24. van Impel, A., Schumacher, S., Draga, M., Herz, H.-M., Grosshans, J., and Müller, H.A.J. (2009). Regulation of the Rac GTPase pathway by the multifunctional Rho GEF Pebble is essential for mesoderm migration in the Drosophila gastrula. Development *136*, 813–822.
25. Gabay, L., Seger, R., and Shilo, B.Z. (1997). MAP kinase in situ activation atlas during Drosophila embryogenesis. Development *124*, 3535–3541.

26. Klingseisen, A., Clark, I.B.N., Gryzik, T., and Müller, H.-A.J. (2009). Differential and overlapping functions of two closely related Drosophila FGF8-like growth factors in mesoderm development. Development *136*, 2393–2402.

27. McMahon, A., Supatto, W., Fraser, S.E., and Stathopoulos, A. (2008). Dynamic analyses of Drosophila gastrulation provide insights into collective cell migration. Science *322*, 1546–1550.

28. Leptin, M., Bogaert, T., Lehmann, R., and Wilcox, M. (1989). The function of PS integrins during Drosophila embryogenesis. Cell *56*, 401–408.

29. Carmena, A., Gisselbrecht, S., Harrison, J., Jiménez, F., and Michelson, A.M. (1998). Combinatorial signaling codes for the progressive determination of cell fates in the Drosophila embryonic mesoderm. Genes Dev. *12*, 3910–3922.

30. Martin, A.C., Kaschube, M., and Wieschaus, E.F. (2009). Pulsed contractions of an actin-myosin network drive apical constriction. Nature *457*, 495–499.

31. Rauzi, M., Krzic, U., Saunders, T.E., Krajnc, M., Ziherl, P., Hufnagel, L., and Leptin, M. (2015). Embryo-scale tissue mechanics during Drosophila gastrulation movements. Nat. Commun. *6*, 8677.

32. Martin, A.C., Gelbart, M., Fernandez-Gonzalez, R., Kaschube, M., and Wieschaus, E.F. (2010). Integration of contractile forces during tissue invagination. J. Cell Biol. *188*, 735–749.

33. Kölsch, V., Seher, T., Fernandez-Ballester, G.J., Serrano, L., and Leptin, M. (2007). Control of Drosophila gastrulation by apical localization of adherens junctions and RhoGEF2. Science *315*, 384–386.

34. Lee, T., and Luo, L. (1999). Mosaic analysis with a repressible cell marker for studies of gene function in neuronal morphogenesis. Neuron *22*, 451–461.

35. Lecuit, T. (2004). Junctions and vesicular trafficking during Drosophila cellularization. J. Cell Sci. *117*, 3427–3433.

36. Lecuit, T., and Wieschaus, E. (2000). Polarized insertion of new membrane from a cytoplasmic reservoir during cleavage of the Drosophila embryo. J. Cell Biol. *150*, 849–860.

37. Laprise, P., and Tepass, U. (2011). Novel insights into epithelial polarity proteins in Drosophila. Trends Cell Biol. *21*, 401–408.

38. Tepass, U., Theres, C., and Knust, E. (1990). crumbs encodes an EGF-like protein expressed on apical membranes of Drosophila epithelial cells and required for organization of epithelia. Cell *61*, 787–799.

39. Harris, T.J.C., and Peifer, M. (2004). Adherens junction-dependent and -independent steps in the establishment of epithelial cell polarity in Drosophila. J. Cell Biol. *167*, 135–147.

40. Cherbas, L., Willingham, A., Zhang, D., Yang, L., Zou, Y., Eads, B.D., Carlson, J.W., Landolin, J.M., Kapranov, P., Dumais, J., et al. (2011). The transcriptional diversity of 25 Drosophila cell lines. Genome Res. *21*, 301–314.

41. Kono, K., Yoshiura, S., Fujita, I., Okada, Y., Shitamukai, A., Shibata, T., and Matsuzaki, F. (2019). Reconstruction of Par-dependent polarity in apolar cells reveals a dynamic process of cortical polarization. eLife *8*, e45559.

42. Sato, M., and Kornberg, T.B. (2002). FGF is an essential mitogen and chemoattractant for the air sacs of the Drosophila tracheal system. Dev. Cell *3*, 195–207.

43. Roy, S., Hsiung, F., and Kornberg, T.B. (2011). Specificity of Drosophila cytonemes for distinct signaling pathways. Science *332*, 354–358.

44. Sohr, A., Du, L., Wang, R., Lin, L., and Roy, S. (2019). *Drosophila* FGF cleavage is required for efficient intracellular sorting and intercellular dispersal. J. Cell Biol. *218*, 1653–1669.

45. Yie, J., Hecht, R., Patel, J., Stevens, J., Wang, W., Hawkins, N., Steavenson, S., Smith, S., Winters, D., Fisher, S., et al. (2009). FGF21 N- and C-termini play different roles in receptor interaction and activation. FEBS Lett. *583*, 19–24.

46. Micanovic, R., Raches, D.W., Dunbar, J.D., Driver, D.A., Bina, H.A., Dickinson, C.D., and Kharitonenkov, A. (2009). Different roles of N- and C- termini in the functional activity of FGF21. J. Cell. Physiol. *219*, 227–234.

47. Erben, R.G. (2016). Update on FGF23 and Klotho signaling. Mol. Cell. Endocrinol. *432*, 56–65.

48. Goldfarb, M. (2005). Fibroblast growth factor homologous factors: evolution, structure, and function. Cytokine Growth Factor Rev. *16*, 215–220.

49. Goldfarb, M. (2001). Signaling by fibroblast growth factors: the inside story. Sci. STKE *2001*, pe37.

50. Popovici, C., Fallet, M., Marguet, D., Birnbaum, D., and Roubin, R. (2006). Intracellular trafficking of LET-756, a fibroblast growth factor of C. elegans, is controlled by a balance of export and nuclear signals. Exp. Cell Res. *312*, 1484–1495.

51. Roubin, R., Naert, K., Popovici, C., Vatcher, G., Coulier, F., Thierry-Mieg, J., Pontarotti, P., Birnbaum, D., Baillie, D., and Thierry-Mieg, D. (1999). let-756, a C. elegans fgf essential for worm development. Oncogene *18*, 6741–6747.

52. Käll, L., Krogh, A., and Sonnhammer, E.L.L. (2004). A combined transmembrane topology and signal peptide prediction method. J. Mol. Biol. *338*, 1027–1036.

53. Edgar, R.C. (2004). MUSCLE: multiple sequence alignment with high accuracy and high throughput. Nucleic Acids Res. *32*, 1792–1797.

54. Gouy, M., Guindon, S., and Gascuel, O. (2010). SeaView version 4: a multiplatform graphical user interface for sequence alignment and phylogenetic tree building. Mol. Biol. Evol. *27*, 221–224.

55. Bownes, M., and Hames, B.D. (1977). Accumulation and degradation of three major yolk proteins in Drosophila melanogaster. J. Exp. Zool. *200*, 149–156.

56. Gavin, J.A., and Williamson, J.H. (1976). Synthesis and deposition of yolk protein in adult Drosophila melanogaster. J. Insect Physiol. *22*, 1457–1464.

57. Bischof, J., Maeda, R.K., Hediger, M., Karch, F., and Basler, K. (2007). An optimized transgenesis system for Drosophila using germ-line-specific phiC31 integrases. Proc. Natl. Acad. Sci. USA *104*, 3312–3317.

58. Sutherland, D., Samakovlis, C., and Krasnow, M.A. (1996). branchless encodes a Drosophila FGF homolog that controls tracheal cell migration and the pattern of branching. Cell *87*, 1091–1101.

59. Pfeiffer, B.D., Ngo, T.-T.B., Hibbard, K.L., Murphy, C., Jenett, A., Truman, J.W., and Rubin, G.M. (2010). Refinement of tools for targeted gene expression in Drosophila. Genetics *186*, 735–755.

60. Lehmann, R., and Tautz, D. (1994). In situ hybridization to RNA. Methods Cell Biol. *44*, 575–598.

61. Blankenship, J.T., Backovic, S.T., Sanny, J.S.P., Weitz, O., and Zallen, J.A. (2006). Multicellular rosette formation links planar cell polarity to tissue morphogenesis. Dev. Cell *11*, 459–470.

62. Miller, K.G., Field, C.M., and Alberts, B.M. (1989). Actin-binding proteins from Drosophila embryos: a complex network of interacting proteins detected by F-actin affinity chromatography. J. Cell Biol. *109*, 2963–2975.

STAR★METHODS

KEY RESOURCES TABLE

REAGENT or RESOURCE	SOURCE	IDENTIFIER
Antibodies		
RFP	MBL International	Cat# PM005; RRID: AB_591279
FLAG	Cell Signaling Technologies	Cat# 2368; RRID: AB_2217020
GFP (rabbit)	Life Technologies	Cat# A-11122; RRID: AB_221569
GFP (goat)	Rockland Immunochemicals	Cat# 600-101-215; RRID: AB_218182
Hb	David Kosman	N/A
Twi (guinea pig)	In house	N/A
Twi (rat)	In house	N/A
Pyr^{intra} guinea pig	This study	N/A
Pyr^{intra} chicken	This study	N/A
Htl	This study	N/A
En	DSHB	Cat# 4D9 anti-engrailed/invected; RRID: AB_528224
Mys	DSHB	Cat# cf.6g11; RRID: AB_528310
Eve	DSHB	Cat# 2b8; RRID: AB_528230
dpERK	Sigma	Cat# M9692; RRID: AB_260729
Beta-Galactosidase	MP Biomedicals	Cat# 559761; RRID: AB_2687418
Armadillo	DSHB	Cat# N2 7A1 ARMADILLO; RRID: AB_528089
Crumbs (Crb)	DSHB	Cat# cq4; RRID: AB_528181
Neurotactin (Nrt)	DSHB	Cat# BP 106 anti-Neurotactin; RRID: AB_528404
Baz	Jennifer Zallen	N/A
Htl (guinea pig)	This study	N/A
Biotinylated anti-chicken	Vector Laboratories	Cat# BA-9010; RRID: AB_2336114
Biotinylated anti-rabbit	Vector Laboratories	Cat# BA-1000; RRID: AB_2313606
Biotinylated anti-mouse	Vector Laboratories	Cat# BA-2000; RRID: AB_2313581
Biotinylated anti-guinea pig	Vector Laboratories	Vector Laboratories Cat# BA-7000; RRID: AB_2336132
Alexa Fluor 488 goat anti-guinea pig	Molecular Probes	Cat# A-11073; RRID: AB_2534117/Lot 1458631
Alexa Fluor 555 donkey anti-mouse	Molecular Probes	Cat# A-31570; RRID: AB_2536180/Lot 1984063
Alexa Fluor 647 goat anti-guinea pig	Molecular Probes	Cat# A-21450; RRID: AB_141882/Lot 1711474
Alexa Fluor 555 goat anti-chicken	Thermo Fisher Scientific	Cat# A-21437; RRID: AB_2535858/Lot 1889319
Alexa Fluor 555 donkey anti-rabbit	Molecular Probes	Cat# A-31572; RRID: AB_162543/Lot 1945911
Alexa Fluor 647 donkey anti-mouse	Molecular Probes	Cat# A-31571; RRID: AB_162542/Lot 1984047
Goat anti-mouse IgG, HRP conjugate	Millipore	Millipore Cat# 12-349; RRID: AB_390192/Lot DAM1518979
Chemicals, Peptides, and Recombinant Proteins		
MBP-Pyr452-715 (Pyr[intra])	This study	Antibody antigen
DAPI	Invitrogen	Cat# D3571; RRID: AB_2307445
TSA Cyanine 3 System	Perkin Elmer	Cat# NEL704A001KT; RRID: AB_2572409/Lot 1845144
Critical Commercial Assays		
VECTASTAIN Elite ABC	Vector Laboratories	Cat# PK-6100; RRID: AB_2336819
Effectene Transfection Reagent	QIAGEN	301425
Experimental Models: Cell Lines		
S2	ATCC	Cat# CRL-1963; RRID: CVCL_Z232
S2-mCh Pyr 1-766 3xFLAG pActPURO	This study	N/A

(*Continued on next page*)

Continued

REAGENT or RESOURCE	SOURCE	IDENTIFIER
Experimental Models: Organisms/Strains		
pyr^{399}	This study	N/A
Pyr^{430}	This study	N/A
Pyr^{680}	This study	N/A
Pyr^{715}	This study	N/A
UASt-*pyr*$^{431-766}$	This study	N/A
UAS-*pyr*$^{1-766}$	[4]	N/A
Df(2R)pyr^{36}	[15]	N/A
UAS-*ths*	[4]	N/A
UASt-*pyr*$^{1-466}$	[5]	N/A
Oregon R	BDSC	2376
yw	N/A	N/A
Tublin-GAL4	[34]	Bloomington 5138
Recombinant DNA		
pMT-PURO	David Sabatini	RRID: Addgene_17923
pACT-PURO	This study	N/A
Bnl EST	DGRC	GH08887
myc-Baz/Par3-mKate2	[41]	Fumio Matsuzaki
Software and Algorithms		
Zen 3.0 (blue edition)	Zeiss	N/A
Imaris 9.0	Bitplane	N/A

RESOURCE AVAILABILITY

Lead Contact

Further information and requests for resources and reagents should be directed to and will be fulfilled by the Lead Contact, Angelike Stathopoulos (angelike@caltech.edu).

Materials Availability

All unique/stable reagents generated in this study, including fly stocks, are available from the Lead Contact without restriction.

Data and Code Availability

This study did not generate large datasets/code, but images used for quantitative analyses are available from the corresponding author upon request.

EXPERIMENTAL MODEL AND SUBJECT DETAILS

Transgenic flies and CRISPR/Cas9 mutagenesis

Pyr aa431-766 (with CAAC ATG added 5′ of the coding sequence to provide translation start context) and Pyr aa1-766 were cloned into pUAS-t attB [57] and inserted into attP site 86Fb (BDSC #24749) via phiC31-mediated recombination and screened for w^+.

Site-specific mutants in Pyr were generated via CRISPR/Cas9, utilizing homology cassettes with a 3xP3 > dsRed marker originating from from pScarlessHD-DsRed flanked by inverted piggyBac transposon inverted repeats assembled in pBluescript. Two stop codons were encoded at each truncation site to prevent readthrough (TAG TAA). DNA encoding dual gRNAs targeting the Pyr locus in pCFD5 was co-injected with each homology cassette into vasa-Cas9 embryos (BDSC #51324). Integrations were identified via 3xP3 > dsRed expression. All microinjections were carried out in-house. The 3xP3 > dsRed cassettes with piggyBAC inverted terminal repeats were removed via chromosomally-supplied piggyBac transposase (BDSC stock #8283). Pyr^{N+C} is a spurious mutation generated during CRISPR/Cas9 mutagenesis of inserting a LexA tag into Pyr between amino acids 456,457. It results from a one base pair deletion of the first cytosine of the codon encoding H295 (likely due to faulty homology directed repair at the site of one of the gRNAs used). A frameshift results in an early termination codon after 28 frameshifted amino acids. In effect, this separates Pyr into the forward-signaling/Htl-binding N-terminal fragment and Pyr^{intra} with the LexA tag. Pyr^{intra} expression is likely the result of internal initiation of translation from an in-frame start codon 3′ of the resulting stop codon. All mutations and precise, ‘‘scarless’’ excisions of the marker cassette, and were sequence-verified by PCR off of genomic DNA of homozygous mutant stocks.

pScarlessHD-DsRed was a gift from Kate O'Connor-Giles (Addgene plasmid #64703; https://www.addgene.org/64703/). pCFD5 was a gift from Simon Bullock (Addgene plasmid #73914; https://www.addgene.org/73914/).

Fly stocks and survival assay

Flies are maintained at 25°C according to standard procedures. *yw* or Oregon R are used as wild-type controls. *tub-GAL4* (#5138) [34] was obtained from Bloomington *Drosophila* Stock Center. *Df(2R)pyr36*, UAS-*ths*, UAS-*pyr* and UAS-pyr^{1-466} have been previously described [4, 5, 17]. UAS-$pyr^{431-766}$ was generated for this study, as described above.

For the survival experiment, 5 males from *yw* or *pyr* mutant stocks were crossed with 5 *Df(2R)pyr36* virgin females. Parents were kept in vials for one week. Eclosed transheterozygous adult flies from each cross were counted and percentage of those ones in *trans* to *Df(2R)pyr36* was calculated to compare the quality of survival.

Cell culture

S2 cells (ATCC CRL-1963) were maintained in Schneider's medium (Life Technologies) supplemented with 10% FBS (HyClone Standard FBS, heat-inactivated) at 25°C. Cells were plated to 1.2x10^6/ml and allowed to adhere before transfection with Effectene (QIAGEN) at ratios of 400ng DNA/3.2ul enhancer/8ul Effectene/ml of cells). $CuSO_4$ was added to 100uM-200uM to the medium at transfection, and cells/supernatants harvested between 60 and 70 hours post-transfection.

The actin 5C promoter was introduced in the place of the metallothionein promoter of pMT-PURO for constitutive expression (''pACT-PURO'') when indicated for 6xHis+mCh < Pyr1-766 > 3xFLAG. Stable lines were generated by linearization of plasmids with ScaI or NsiI, transfected using the protocol above, incubated for ~72 hours, and passaged 1:5 into fresh media with puromycin (Invivogen ant-pr-1) at 1 ug/ml. After 3-4 days, cells were passaged 1:5 again, and split 3-4 more times at intervals of 3-5 days before being taken off of antibiotic two passages before experiments.

METHOD DETAILS

Plasmids and clones

Most tissue culture experiments were performed with a derivative of pMT-PURO (Addgene #17923, a gift from David Sabatini) with an augmented MCS and other modifications to the vector to accommodate the tags and gene fragments used (details available upon request). The 6xHis+mCh tag was introduced after the signal peptide for both Pyr (between aa 30, 31) and Ths (between aa 22, 23) with a Gly-Ser-Ser linker at the cassette boundaries. BDSC clone GH08887 was used for cloning of the non-TMD isoform (Bnl-C, also identical to protein sequence of Bnl-D). The TMD present in Bnl-A was added by overlap PCR using published mRNA sequence to match the original cDNA identified [58]. The GFP used is *Drosophila* codon-optimized GFP [59] with the monomeric A206K mutation introduced in our lab.

Pulldown of FGFs from cell culture supernatants

Supernatants were spun 3x at 200 g for 2.5 minutes, moving the supernatant to a new tube with each spin, carefully avoiding cell pellets and floating cells. Supernatants were mixed 1:1 with 2X pulldown buffer (final concentration 20 mM sodium phosphate pH 7.4, 300 mM NaCl, 0.1% NP-40, 10 mM imidazole, 5% glycerol, 14 mM mercaptoethanol), and incubated in batch with 30ul of Ni-NTA beads (QIAGEN) for 1 hour at 4°C with gentle agitation. Beads were collected and washed 2x with 1x binding buffer. Bound proteins were eluted with 150ul of 1x SDS sample buffer at 85C for 5 minutes. Cell pellets were washed with PBS, then lysed in PBS pH 7.4 with 6M Urea and 0.5% CHAPS supplemented with Complete Protease Inhibitor and PhosStop (Roche), spun to remove cellular debris, and mixed with an equal volume of 2X SDS sample buffer. Extracts were subjected to 8 - 10% SDS-PAGE, blotted onto PVDF (Immobilon-P, Millipore) or nitrocellulose (Whatman BA85) and blocked with 0.2% BSA in TBST for 5 min. Blots were incubated overnight at 4°C with antibodies against RFP (MBL PM005, 1:2000), GFP (Life technologies A11122 1:2000), FLAG/DYKDDDDK (Cell Signaling Technologies #2368, 1:2000), Blots were incubated with HRP-conjugated secondary antibodies for 1 hour. Five washes of 5-10 minutes with TBST were used, depending on the antibody, and developed with ProSignal Dura ECL reagent (Genesee Scientific 20-301) using HyBlot CL Autoradiography Film (Denville Scientific).

Generation of anti-Pyr^{intra} antibodies

Anti-Pyr^{intra} was generated from an MBP fusion to Pyr amino acids 452-715 (in pMAL-c2x, NEB) and purified according to the manufacturer's protocol. Antigen was sent to Pocono Rabbit Farm and Laboratory for sera production in chicken and guinea pig. Sera were depleted of anti-MBP antibodies prior to affinity purification. Antibodies were affinity-purified using the original antigen (conjugated to Aminolink or Aminolink Plus beads, per the manufacturer's protocol). Antibodies were pre-absorbed with embryos, and in the case of anti-Pyr^{intra}, pre-absorbed with Pyr^{1-430} mutants.

Immunoprecipitation

Affinity-purified guinea pig α-Pyr^{intra} was conjugated to Protein-G beads with dimethyl pimelimidate as detailed (https://www.neb.com/protocols/1/01/01/cross-linking-of-igg-to-protein-a-or-g-beads). 3-7 hour embryos or PBS-washed S2 cells were dounce homogenized in 50 mM HEPES pH 7.5, 150mM NaCl, 5% glycerol, 0.1% NP-40, supplemented with Complete Protease Inhibitor and PhosStop Phosphatase Inhibitor. Extracts were spun at 13,000xg for 20 minutes. Extracts were pre-cleared with unconjugated

beads to reduce non-specific binding, but did little to deplete the prominent ~48kDa band band, which is not present in immunoprecipitates from S2 cell extracts. The supernatant was incubated with the antibody-conjugated beads or beads alone for 1.5 hour at 4C with gentle mixing. Unbound material was removed, and the beads washed 2X with lysis buffer. The immunoprecipitated material was eluted into 1X SDS sample buffer and subjected to 9% SDS-PAGE, transferred to BA85 membrane as above, and probed with affinity-purified chicken α-Pyr^{intra} antibody. Guinea pig anti-Pyr^{intra} was used for IP, and chicken anti-Pyr^{intra} for detection. Beads without antibody are used as a negative control from wild-type embryo extract, and also IP from parallel extracts of Pyr mutant embryos that completely lack Pyr^{intra} (Pyr^{430}).

Whole mount *in situ* hybridization, immunohistochemistry and immunofluorescence

Digoxigenin (DIG) labeled antisense RNA probe against *pyr* coding sequence PCR product, amplified from genomic DNA [4]. *In situ* hybridization was performed as previously described [60]. An anti-DIG antibody conjugated with Alkaline phosphatase (1:500, Sigma, 11093274910) along with the substrates NBT/BCIP (Roche) were used to visualize the signal.

Antibody staining was carried out as previously described using fixation conditions appropriate for epitopes to be assayed. Standard 4% formaldehyde fixation was used for staining with antibodies against Hb (1:300, guinea pig, a gift from D. Kosman), En (1:50, DSHB, 4D9), Twi (1:200, guinea pig or rat, produced in house), Mys (1:25, DSHB *CF.*6G11), Eve (1:50; DSHB 2B8), dpERK (1:400, Sigma M9692, amplified by TSA, Perkin Elmer), β-gal (1:2000, MP Biomedicals) or GFP (1:5000, Rockland Immunochemicals, 600-103-215). Embryos stained with Pyr^{intra} (1:200, chicken or guinea pig, produced in house), Arm (1: 40, DSHB, N2 7A1), Nrt (1:50, DSHB, BP106), Crb (1:40, DSHB, Cq4), Baz (1:500, a gift from Dr. Jennifer Zallen, Sloan Kettering Institute, USA, [61]) or Htl (1:500, guinea pig, produced in house) were heat-methanol fixed as described [62]. VECTASTAIN Elite ABC system was used in combination with biotinylated secondary antibodies (Vector Laboratories anti-chicken BA9010, anti-rabbit BA1000, anti-mouse BA-2000, anti-guinea pig BA-7000) and DAB substrate to develop immunohistochemistry signals. For immunofluorescence, Alexa Fluor 488, 555 and 647 secondary antibodies were used (1:500, Molecular Probes).

Plastic sectioning of embryos, and imaging fluorescent signals

Embryos were mounted in Permount (Fisher Scientific) for whole-mount studies or embedded in araldite (Electron Microscopy Sciences) for cross-sectioning. Plastic sections (8-10 μm) were obtained using a rotary microtome (MR3, RMC Boeckeler) and mounted in 1:1 acetone: araldite solution. Images were taken with Axio Imager Z2 microscope and Axiocam 506 camera (Zeiss). 40X objective was used for sections and 20X for whole mount embryos. *Z*-stacks were obtained for *pyr in situ* annf Pyr^{intra} whole mount staining under Zen 3.0 blue edition software (Zeiss) and the orthogonal projections function was used to produce the representative images.

Embryos were cleared in 70% glycerol and manually picked and positioned on slides prior to fluorescence imaging with LSM 800 laser scanning confocal microscope (Zeiss). Both 25X and 40X objectives were used.

S2 cell assay of Baz polarization

Drosophila cultured S2 cells were co-transfected as above with myc-Baz-mKate2 [41] and the indicated mCh < Pyr > GFP constructs as above, and induced at 1mM $CuSO_4$ for 2-3 days, when Baz expression began to peak. Cells were plated onto concanavalin-A treated coverslips below surface confluence, allowed to adhere for 10-15 minutes, and washed twice with fresh media containing $CuSO_4$, mounted via hanging drop, incubated for 4-5 hours, and visualized live with fluorescent microscopy with a Zeiss Axioimager Z.2 with Plan-apochromat 63x oil immersion objective (aperture 1.4), and filters of: 43 He mCh/mKate2 BP 538-562nm, 38 He GFP fluorescent protein, 450-490nm. Only bright cells with clear Baz expression were assayed. Ambiguous Baz localization due to uneven adherence to the coverslip, multipolar cells, and low expression were not considered. The red channel signal was a combination of both myc-Baz-mKate2 and mCh < Pyr > GFP.

Tethering of mCh-Pyr to the plasma membrane with TMDs

6xHis,mCh Pyr1-292 was fused to 3xFLAG, the TMD of CD2, the Pyr TMD with additional adjacent sequence (aa 386-440), aa 631-770 of Bnl-A, and aa 631-660 of Bnl-C and transfected into S2 cells as above. This assay was used since Bnl-A tagged at its C terminus with GFP did not show membrane localization, likely due to there being only several amino acids following its TMD, and addition of a C-terminal GFP Bnl-A protein disrupts the TMD prediction. Cells were plated onto slides, incubated, and imaged identically to those for measuring Baz polarization.

QUANTIFICATION AND STATISTICAL ANALYSIS

Secondary structure prediction and multiple sequence alignments of Pyr

Accession numbers for Pyr orthologs used in multi-sequence alignments: *Drosophila melanogaster* NM_001103805.2, *Drosophila* yakuba XP_002091178.2, *Drosophila* willistoni XP_023033665.1, *Drosophila* grimshawi XP_001994979.1, *Drosophila* virilis XM_002049174.2, Bactrocera oleae/olive fruit fly XP_014089211.1, Bactrocera cucurbitae/melon fly XP_011190593.1, Ceratitis capitata/medfly XP_012160819.2, Musca domestica/housefly XP_011294469.2, Stomoxys calcitrans/stable fly XP_013100312.1. Alignments were performed using MUSCLE [53] for Pyr orthologs in SEAVIEW software ([54], http://doua.prabi.fr/software/seaview). Color codes for amino acids are: hydrophobic/blue, polar/green, basic/red, acidic/purple, proline/yellow, and glycine/orange. Phobius http://phobius.sbc.su.se/ [52] was used for signal peptide and transmembrane domain predictions. Using

hydrophobicity and helix prediction, it identifies these amphipathic helices, and differentiates between the two based on amino acid context following the helix, and reports a continuous probability (posterior label probability) along the polypeptide of the possible states of signal peptide, secreted fraction, transmembrane domain, and cytoplasmic fraction. 1 is the highest score/probability. Graphs in main figures were traced from the original .png file provided by the website output for visual clarity.

Quantification of the mesoderm protrusions, dpERK positive cells and immunofluorescence of Mys, Pyr^{intra} and Arm

Protrusions quantification was carried out in Zen blue (Zeiss) with images of embryos stained with a Htl antibody. Length was determined under graphic--->distance--->length by drawing a line from the tip of protrusion to the nucleus. Protrusions shorter than 6 μm were not included in quantification.

Quantification of dpERK positive cells was done with Imaris 9.0 software (Bitplane). Briefly, 70∼80 μm z stacks were obtained by imaging the embryos from the ventral side, reconstructed 3D images were then smoothed using a Gaussian filter. Only the middle portion of the embryo image along the AP axis was analyzed. Spot-selection was achieved by first using a channel filter to select mesoderm cells that were stained by Twi antibody, then a second channel filter was used to select mesoderm cells that were also dpERK-positive. A minimum of 6 embryos at stage 8 were imaged and analyzed for each genotype. Shapiro-Wilk normality test and Student's t test were used.

To quantify the immunofluorescent signal for Mys or Pyr^{intra}, embryos were cross-sectioned with razor blades to remove the anterior and posterior $^1/_3$ portions, leaving the middle regions mounted in 70% glycerol. Imaging and quantification were both done with Zen blue edition (Zeiss). Briefly, a 30 μm *z*-stack was acquired and an average orthogonal projection was made from 12 slices of approximately 24 μm scan. Relative levels of fluorescent signal were calculated by dividing the intensity mean value of a selected ROI by a background value (ventral ectoderm for Mys and dorsal ectoderm for Pyr^{intra}) of the same size measured under Graphic/Rectangle tool. For Mys staining, 8 measurements of relative signal intensity were taken from 4 embryos and subjected for Shapiro-Wilk normality test. For Pyr^{intra} staining, an average was first calculated for each individual and data from 8 embryos were put to normality test. Student's t test was used to examine the difference in mean.

Cross sections of embryos stained with an Arm antibody were mounted as described above and single scans were obtained. With Zen, clusters of Arm-positive puncta were selected via graphic--->rectangle and the mean intensity values were calculated for regions of 1.5 × 5 μm in size at both the apical and basal junction domains along the lateral membrane. An average ratio was calculated for each embryo from at minimum 10 pairs of apical/basal values. Data exhibit normal distribution. Significance is reached in t test with 3 embryos for each genotype.